

This document is confidential and is proprietary to the American Chemical Society and its authors. Do not copy or disclose without written permission. If you have received this item in error, notify the sender and delete all copies.

**Observation of  $[V_{Cu}^{1-} In_i^{2+} V_{Cu}^{1-}]$  defect triplets in Cu-deficient  $CuInS_2$**

Journal:	<i>The Journal of Physical Chemistry</i>
Manuscript ID	jp-2020-08872a.R1
Manuscript Type:	Special Issue Article
Date Submitted by the Author:	05-Nov-2020
Complete List of Authors:	Frick, Jessica; Princeton University, Department of Chemistry; Stanford University, Aeronautics & Astronautics Cheng, Guangming; Princeton University, PRISM Kushwaha, Satya; Los Alamos National Laboratory, Yao, Nan; Princeton University, Materials Institute Wagner, Sigurd; Princeton University, Electrical engineering Bocarsly, Andrew; Princeton University, Chemistry Cava, Robert; Princeton University, Dept. of Chemistry

SCHOLARONE™  
Manuscripts

# Observation of $[V_{Cu}^{1-} In_i^{2+} V_{Cu}^{1-}]$ Defect Triplets in Cu-Deficient $CuInS_2$

*Jessica J. Frick*<sup>1,\*</sup>, <sup>†</sup>, *Guangming Cheng*<sup>2</sup>, *Satya Kushwaha*<sup>1,†</sup>, *Nan Yao*<sup>2</sup>, *Sigurd Wagner*<sup>3,\*</sup>,  
*Andrew B. Bocarsly*<sup>1</sup>, *Robert J. Cava*<sup>1</sup>

<sup>1</sup> Department of Chemistry, Princeton University, Princeton NJ 08544; <sup>2</sup> PRISM, Princeton University, Princeton NJ 08544; <sup>3</sup> Department of Electrical Engineering, Princeton University, Princeton NJ 08544.

## ABSTRACT

Copper indium disulfide ( $CuInS_2$ ) is a semiconductor with a direct energy band gap of 1.53 eV, an optimal value for highly efficient thin-film solar cells. But it has reached only ~ 11 % power conversion efficiency, far less than the theoretically achievable value of ~ 30 %. The cause of this low performance is not understood. A single crystal grown from 1 mol% Cu-deficient melt was studied, using atomic resolution high-angle annular dark-field (HAADF) scanning transmission electron microscopy (STEM) and electron dispersive spectroscopy (EDS). While the bulk crystal is exactly stoichiometric  $CuInS_2$ , it contains nanometer-thick, structurally coherent, Cu-deficient interphases that form along rotational twin boundaries in the  $\{112\}$  plane. Transition zones from bulk crystal to interphase are observed, where In is seen to move from its normal site  $In_{In}$  in the chalcopyrite structure to a tetrahedral interstitial site  $In_i$ , while Cu remains in its normal  $Cu_{Cu}$  position. Two  $In_{In}$  rows of the bulk crystal merge into one row of  $In_i$ , causing excess  $In_i$  in the

1  
2  
3 interphase. The concentrations of  $\text{Cu}_{\text{Cu}}$  and  $\text{In}_i$  reflect a ratio of Cu vacancies,  $V_{\text{Cu}}$ , to excess  $\text{In}_i$  of  
4  
5  $\sim 2$ . Their relative lattice positions, and the high electrical resistivity of the crystal, suggests that  
6  
7  $V_{\text{Cu}}$  and excess  $\text{In}_i$  ‘precipitate’ as self-compensating, electrically neutral,  $[V_{\text{Cu}}^{1-} \text{In}_i^{2+} V_{\text{Cu}}^{1-}]$  defect  
8  
9 triplets. This is the first atomic-level observation of the ordered defect that has been invoked as  
10  
11 the basic structural modifier in chalcopyrite compound homologs. The interphases introduce an  
12  
13 optical gap of 1.47 eV. Electron trapping in band tail states, evident from a photoconductivity  
14  
15 exponent of 0.54, is the likely cause of an unusually low electron mobility of  $0.1 \text{ cm}^2\text{V}^{-1}\text{s}^{-1}$ . The  
16  
17 overall result is that making  $\text{CuInS}_2$  slightly copper-poor inserts nanometer-thick layers of the  
18  
19 interphase into the bulk crystal. This study shows that apparently conflicting results of the effect  
20  
21 of Cu deficiency on  $\text{CuInS}_2$  thin-film solar cells may be resolved by analyzing structure and  
22  
23 composition at nanometer spatial resolution.  
24  
25  
26  
27

## 28 1. INTRODUCTION

29  
30  
31 **1.1 *CuInS<sub>2</sub> thin-film solar cells.***  $\text{CuInS}_2$  is a diamond-like semiconductor with the crystal  
32  
33 structure of chalcopyrite that was first synthesized to explore the applicability to ternary  
34  
35 compounds of the Grimm-Sommerfeld valence rules for tetrahedral coordination.<sup>1-4</sup> The  
36  
37 chalcopyrites have the diamond-like zincblende structure but with two cations ordered on  
38  
39 sublattices. The Bravais lattice of the chalcopyrite is body centered tetragonal, belonging to space  
40  
41 group  $I\bar{4}2d$ . The first crystals of  $\text{CuInS}_2$  were grown to evaluate its suitability for semiconductor  
42  
43 device applications, and for its piezoelectric and non-linear optical properties.<sup>5-7</sup> The direct energy  
44  
45 band gap of  $\text{CuInS}_2$  makes it a strong light absorber, with a value of 1.53 eV that lies at the  
46  
47 optimum for efficient single-junction solar cells.<sup>8,9</sup> Therefore  $\text{CuInS}_2$  has been explored for  
48  
49 polycrystalline thin-film solar cells,<sup>10</sup> beginning with a 3.6% efficient homojunction cell,<sup>11</sup> then *n*-  
50  
51  $\text{CdS}/p\text{-CuInS}_2$  heterojunction solar cells first reaching 7.3%,<sup>12</sup> and later 11.4% power conversion  
52  
53  
54  
55  
56  
57  
58  
59  
60

1  
2  
3 efficiency.<sup>13</sup> What has kept the CuInS<sub>2</sub> efficiency substantially lower than the 15% reached with  
4  
5 CuInSe<sub>2</sub> is not understood.<sup>14</sup> Much higher efficiencies have been reached with alloys of CuInS<sub>2</sub>:  
6  
7 15% by alloying with Ga<sub>2</sub>S<sub>3</sub> in Cu(In,Ga)S<sub>2</sub>,<sup>15</sup> and the highest efficiency achieved in any inorganic  
8  
9 thin-film solar cell of 23.35% with a compositionally graded Cu(In,Ga)(S,Se)<sub>2</sub> alloy absorber  
10  
11 layer.<sup>16</sup>  
12  
13

14  
15 CdTe and Cu(In,Ga)Se<sub>2</sub> thin-film solar panels are deployed on large scales. The  
16  
17 commercial successes of these solar cells made of polycrystalline thin films are the result of  
18  
19 primarily empirical research and development. Controlling electrically active defects and carrier  
20  
21 lifetimes remains an art. Stoichiometry, point and line defects, grain boundaries, and interfaces  
22  
23 affect conductivity type, carrier mobility and recombination lifetime, and thereby solar cell  
24  
25 efficiency. Overall, the quantitative understanding of the electronic properties of polycrystalline  
26  
27 thin-film compound semiconductors is far from that of polycrystalline silicon,<sup>17,18</sup> which grew  
28  
29 from an exhaustive grasp of the properties of single-crystalline silicon. To the device physics  
30  
31 community, it is a given that the quantitative understanding of single-crystal chalcopyrite  
32  
33 semiconductors is indispensable for reaching maximum thin-film solar cell performance.  
34  
35 Therefore, soon after initial exploration,<sup>5-7</sup> raising solar cell efficiency became the principal  
36  
37 motive for studying CuInS<sub>2</sub> single crystals.<sup>19-28</sup> An exemplary single-crystal result is the  
38  
39 measurement of electron mobilities as high as 338 cm<sup>2</sup>/Vs,<sup>22</sup> providing an important yardstick for  
40  
41 assessing the device quality of polycrystalline CuInS<sub>2</sub> films. The goal of the present study was to  
42  
43 resolve a long-standing debate in polycrystalline CuInS<sub>2</sub> solar cells, namely the existence and  
44  
45 presumed effects of Cu-deficiency, by clearly identifying the phase(s) and defects in a CuInS<sub>2</sub>  
46  
47 single crystal grown from a slightly copper-deficient melt.  
48  
49  
50  
51  
52  
53  
54  
55  
56  
57  
58  
59  
60

1  
2  
3 **1.2 Stoichiometry of  $\text{CuInS}_2$ .** Chalcopyrite crystals can be homogeneous at non-  
4 stoichiometries of up to several atomic percentages.<sup>1,29</sup> A finite range of sulfur-content is evident  
5 from the ability to make  $\text{CuInS}_2$  crystals *n*-type by annealing under minimum sulfur pressure, and  
6 *p*-type when annealed at high pressure.<sup>6,9</sup> That allowed the fabrication of an *n-on-p* type  
7 homojunction thin-film cell, made by changing the sulfur pressure from high to low during film  
8 growth.<sup>11</sup> Indeed, adjusting composition instead of substitutionally doping remains the means of  
9 controlling carrier type and magnitude of the electrical conductivity in  $\text{CuInS}_2$ . But the role of Cu  
10 non-stoichiometry in setting the efficiency of polycrystalline thin-film  $\text{CuInS}_2$  solar cells remains  
11 controversial. The search for high efficiency initially explored Cu-poor material,<sup>30</sup> as employed in  
12  $\text{CuInSe}_2$  cells,<sup>31</sup> then moved to Cu-rich  $\text{CuInS}_2$ ,<sup>10,13,30</sup> and then back again to Cu-poor  
13  $\text{Cu}(\text{In,Ga})\text{S}_2$ .<sup>15</sup> Several reports describe depositing  $\text{CuInS}_2$  absorber films with excess Cu, and then  
14 removing that excess by etching in KCN solution prior to heterojunction fabrication, insinuating  
15 substantial solubility of Cu in  $\text{CuInS}_2$ .<sup>10,13,30,32</sup> A recent study illustrates the challenge of  
16 identifying the solar-optimal stoichiometry of  $\text{CuInS}_2$ . Lomuscio et al.<sup>32</sup> prepared  $\text{CuInS}_2$   
17 polycrystalline films with either copper excess or copper deficiency, set by either single or two-  
18 step vacuum deposition under five different temperature protocols. Surprisingly, the quasi-Fermi  
19 level split measured in the films (a gauge of achievable open-circuit voltage) did not correlate with  
20 the open circuit voltage of  $\text{CuInS}_2$  solar cells made from these films. The observation by Klenk et  
21 al.<sup>10</sup> that films with copper-poor compositions exhibit very Cu-deficient free surfaces points to the  
22 possibility of phase separation between  $\text{CuInS}_2$  and a Cu-poor phase. Such phase separation may  
23 also occur at interfaces, as is suggested by the formation of a  $\text{CuIn}_5\text{S}_8$  interlayer by Cu out-  
24 diffusion from a  $\text{Cu}(\text{In,Ga})\text{Se}_2$  absorber near the heterojunction into the overlaying  $\text{In}_x\text{S}_y$  buffer,  
25 which depletes the absorber of Cu.<sup>33</sup> By changing the energy band alignment or the conductivity  
26  
27  
28  
29  
30  
31  
32  
33  
34  
35  
36  
37  
38  
39  
40  
41  
42  
43  
44  
45  
46  
47  
48  
49  
50  
51  
52  
53  
54  
55  
56  
57  
58  
59  
60

1  
2  
3 type at the heterojunction, such depletion can have drastic effects on solar cell efficiency.<sup>34–37</sup>  
4  
5 Therefore, to design the optimal solar cell material it is clearly important to know where the Cu-  
6  
7 poor boundary of CuInS<sub>2</sub> lies, and what the crystal properties at that phase boundary are.  
8  
9

10 **1.3 Phase diagram of CuInS<sub>2</sub>.** Observations made during the first growth of single crystals<sup>5</sup>  
11 suggested that the tetragonal  $\gamma$ -phase of CuInS<sub>2</sub>, which is the stable modification below 980 °C,<sup>23,38</sup>  
12 has a narrow homogeneity range, as was also suggested by the In<sub>2</sub>S<sub>3</sub> and Cu<sub>2-x</sub>S admixtures  
13 detected in evaporated CuInS<sub>2</sub> thin films.<sup>12</sup> While Binsma et al.<sup>38</sup> extrapolated to a narrow Cu-rich  
14 and a wider Cu-poor homogeneity range at room temperature, in the course of a study of the In-  
15 CuInS<sub>2</sub> phase diagram Fearheiley et al.<sup>23</sup> found no appreciable solubility of In (suggesting no  
16 appreciable Cu-deficiency) in CuInS<sub>2</sub>. Verheijen et al.<sup>39</sup> identified a homogeneity range from 50  
17 to 52 mol% In<sub>2</sub>S<sub>3</sub> (i.e., Cu deficiency) in the Cu<sub>2</sub>S-In<sub>2</sub>S<sub>3</sub> binary system. Crystals grown from  
18 stoichiometric melts under temperature gradients > 10 °C/cm contained lamellar structures of  
19 stoichiometric CuInS<sub>2</sub> separated by the highly Cu-deficient thiospinel CuIn<sub>5</sub>S<sub>8</sub>.<sup>24–26,40</sup> The authors  
20 suggest that Cu-deficient CuInS<sub>2</sub> is not stable, and surmise that the formation of CuIn<sub>5</sub>S<sub>8</sub> from  
21 stoichiometric melts indicates that constitutional supercooling is enabled by the dissolution of  
22 Cu<sub>2</sub>S in CuInS<sub>2</sub> (i.e., CuInS<sub>2</sub> can absorb excess Cu<sub>2</sub>S). The summary of this group of investigations  
23 is that stoichiometric CuInS<sub>2</sub> can take up Cu<sub>2</sub>S but not lose it. A crystallographic study of the  
24 compositions of polycrystalline films in the Cu<sub>2</sub>S-In<sub>2</sub>S<sub>3</sub>-Ga<sub>2</sub>S<sub>3</sub> ternary system with focus on Cu-  
25 poor compositions,<sup>41</sup> also concluded that the Cu-poor homogeneity range must be very narrow;  
26 all Cu-poor compositions did result in two-phase mixtures of essentially stoichiometric CuInS<sub>2</sub>  
27 and CuIn<sub>5</sub>S<sub>8</sub>.<sup>42–44</sup>  
28  
29  
30  
31  
32  
33  
34  
35  
36  
37  
38  
39  
40  
41  
42  
43  
44  
45  
46  
47  
48  
49  
50

51 A detailed theoretical study of point defects in CuInSe<sub>2</sub> by density-functional theory by  
52 Zhang et al.<sup>45</sup> suggests that Cu-deficiency is accommodated by the formation of stable, electrically  
53  
54  
55  
56  
57  
58  
59  
60

1  
2  
3 neutral  $[V_{Cu}^{1-} In_{Cu}^{2+} V_{Cu}^{1-}]$  defect triplets; these enable the self-compensation of Cu vacancy  
4  
5 acceptors,  $V_{Cu}$ , by moving In to Cu sites where it becomes the antisite donor  $In_{Cu}$ . The defect  
6  
7 triplets are the basic structural constituent of group-I deficient ordered defect compounds (ODC).  
8  
9  
10 Wasim et al.<sup>46</sup> verified these theoretical findings with a combined experimental and theoretical  
11  
12 study of a group of chalcopyrites and their ODC derivatives. It is important to keep in mind that Cu-  
13  
14 deficiencies introduced in phase diagram studies, or in crystal and thin-film growth, are large by  
15  
16 the standard of electronic substitutional doping. While a 1 at.% deficiency in composition may  
17  
18 produce mostly electrically neutral defects like  $[V_{Cu}^{1-} In_{Cu}^{2+} V_{Cu}^{1-}]$ , it still might leave a minor  
19  
20 (e.g.,  $10^{-4}$  at.%) concentration of electrically active dopant defects, enough to dominate charge  
21  
22 transport in solar cells.  
23  
24  
25

26 In this study we identify the phase(s), the structural, and the opto-electronical properties of  
27  
28 a  $CuInS_2$  crystal grown from a 1 mol% Cu-deficient melt. We describe crystal growth and basic  
29  
30 crystal properties, then the crystal's atomic structure as seen by scanning/transmission electron  
31  
32 microscopy (STEM), plus its fine structure atomically mapped in conjunction with atomic scale  
33  
34 electron dispersive spectroscopy (EDS) for analysis of composition. The crystal's optoelectronic  
35  
36 properties are evaluated by measuring electronic transport and photoconductivity. The results are  
37  
38 fascinating: we discovered a Cu-deficient phase *in statu nascendi*, including the gradual  
39  
40 displacement of In from its normal site in the chalcopyrite to a new site that, while interstitial in  
41  
42 the chalcopyrite, is the dominant position of In in the Cu-deficient phase.  
43  
44  
45

## 46 2. INSTRUMENTATION & METHODS

47  
48  
49 Powder X-ray diffraction analysis was performed on a Bruker D8 Advance Eco with Cu K $\alpha$   
50  
51 radiation and a LynxEye-XE detector. The scan parameters were 0.02°/step with 0.085 s/step, for  
52  
53 a total scan time of 8 min. A Quanta 200 field emission gun environmental scanning electron  
54  
55  
56  
57  
58  
59  
60

1  
2  
3 microscope (SEM) equipped with an integrated Oxford System was employed for energy  
4 dispersive X-ray (EDS) analysis, for routine evaluation of chemical constituents. X-ray  
5 photoelectron spectra (XPS) were collected under  $10^{-9}$  Torr using a ThermoFisher K-Alpha X-ray  
6 photoelectron spectrometer. All spectra were recorded using Al  $K\alpha$  radiation (1487 eV) with a  
7 survey and pass energy of 100 and 20 eV, respectively. Measured peaks were fit using Casa XPS  
8 software and a Shirley background. The C 1s peak at 284.5 eV of adventitious hydrocarbon was  
9 used as an internal binding energy reference. The optical bandgap was measured with the Agilent  
10 Technologies Cary 5000 UV-Vis-NIR spectrometer equipped with a Universal Measurement  
11 Accessory (UMA) with incident light from 200 to 1300 nm wavelength.  
12  
13  
14  
15  
16  
17  
18  
19  
20  
21  
22  
23

24 Photoconductivity measurements were performed on the same instrument as the electronic  
25 transport measurements, a Quantum Design Physical Property Measurement System, using a  
26 custom dark-room setup. Ohmic contact was made with Pt wires connected to the (112) surface  
27 with InGa eutectic. Current-voltage curves were plotted in real time as the potential was swept  
28 between -10 and 10 V at varying LED light intensities with each wavelength tested (365 nm, 395  
29 nm, 462 nm, 537 nm, 640 nm, 780 nm, 850 nm, 940 nm, and 1050 nm). These measurements were  
30 performed at room temperature.  
31  
32  
33  
34  
35  
36  
37  
38  
39

40 The resulting, symmetric I-V curves demonstrate ohmic behavior at both wire contact points  
41 showing that non-ohmic contacts are not the origin of the observed effects. The linear slope of the  
42 I-V curves indicate that the system's free electron lifetime remains constant, given the relationship:  
43  
44  
45  $I = e \frac{F\mu\tau}{L^2} V$  where  $e$  is the electron charge,  $F$  is the free electron generation rate,  $\mu$  is the mobility,  $\tau$   
46 is the free electron lifetime, and  $L$  is the spacing of electrodes.  
47  
48  
49  
50  
51

### 52 3. EXPERIMENT & RESULTS

53  
54  
55  
56  
57  
58  
59  
60



1  
2  
3 **3.1 Single crystal growth and initial characterization.** Polycrystalline  $\text{Cu}_{0.99}\text{In}_{1.00}\text{S}_{2.00}$ , (i.e., 1  
4 mol% Cu deficient) was synthesized from the elements Cu (99.99%), In (99.999%), and S  
5 (99.99%) in an evacuated quartz tube at  $T = 1100\text{ }^\circ\text{C}$ .<sup>47</sup> After ascertaining the chalcopyrite structure  
6 by powder X-ray diffraction, and composition by energy-dispersive X-ray spectroscopy (EDS), ~  
7 20 g were ground into large grains and sealed under vacuum in a carbon-coated quartz tube. The  
8  $\text{CuInS}_2$  single crystal was grown in a vertical Bridgman furnace set to  $1140\text{ }^\circ\text{C}$ . The quartz tube  
9 was held in the hot zone for 24 hours, then lowered through the length of the furnace at 0.1  
10 mm/hour, and finally annealed at  $T = 400\text{ }^\circ\text{C}$  for 24 hours. This annealing temperature  
11 approximates the substrate temperatures in films deposited by thermal evaporation of the  
12 elements.<sup>32,41</sup> The four independent variables—stipulated by the phase rule for setting the  
13 composition of a ternary compound—are temperature, total pressure, sulfur partial pressure and  
14 copper-to-indium ratio.<sup>23,48–50</sup>

15  
16  
17  
18  
19  
20  
21  
22  
23  
24  
25  
26  
27  
28  
29  
30  
31 During extraction from the quartz tube, the 38 mm long single crystal ingot cleaved  
32 along the (112) plane into six pieces (Fig. 1a). All further measurements were made on the section  
33 IV piece, ~ 14 mm from the tip of the ingot. We cleaved four different samples for evaluating  
34 optical, X-ray, TEM, and photoconductivity characteristics. The freshly cleaved samples were not  
35 chemically etched prior to measurement. The material's optical transmission spectrum (Fig. 1b)  
36 exhibits the steep absorption edge of a direct-gap semiconductor, from which we extract an optical  
37 band gap of 1.47 eV. Figure 1c shows the XRD patterns of the (112) face of a  $\text{CuInS}_2$  crystal and  
38 of a powder sample prepared from the crystal boule, and the corresponding database pattern. The  
39 diffraction lines are not broadened, as they might be by small domains. Laue diffraction identifies  
40 the crystal's natural cleavage plane as (112) (inset to Fig. 1c), powder XRD confirms the tetragonal  
41 chalcopyrite structure (space group  $I\bar{4}2d$ ). X-ray photoelectron spectroscopy (XPS) confirmed  
42  
43  
44  
45  
46  
47  
48  
49  
50  
51  
52  
53  
54  
55  
56  
57  
58  
59  
60

1  
2  
3 Cu<sup>1+</sup> and In<sup>3+</sup> oxidation states as well as an S<sup>2-</sup> sulfide peak (SI, Fig. S1). With scanning electron  
4 microscopy (SEM) we found that the crystal's perimeter—which had been in contact with the  
5 carbon-coated quartz wall—exhibits pronounced (112) terraces, i.e., along the natural cleavage  
6 plane (Fig. 1d and e).<sup>23</sup>  
7  
8  
9  
10  
11  
12  
13  
14  
15  
16  
17  
18  
19  
20  
21  
22  
23  
24  
25  
26  
27  
28  
29  
30  
31  
32  
33  
34  
35  
36  
37  
38  
39  
40  
41  
42  
43  
44  
45  
46  
47  
48  
49  
50  
51  
52  
53  
54  
55  
56  
57  
58  
59  
60

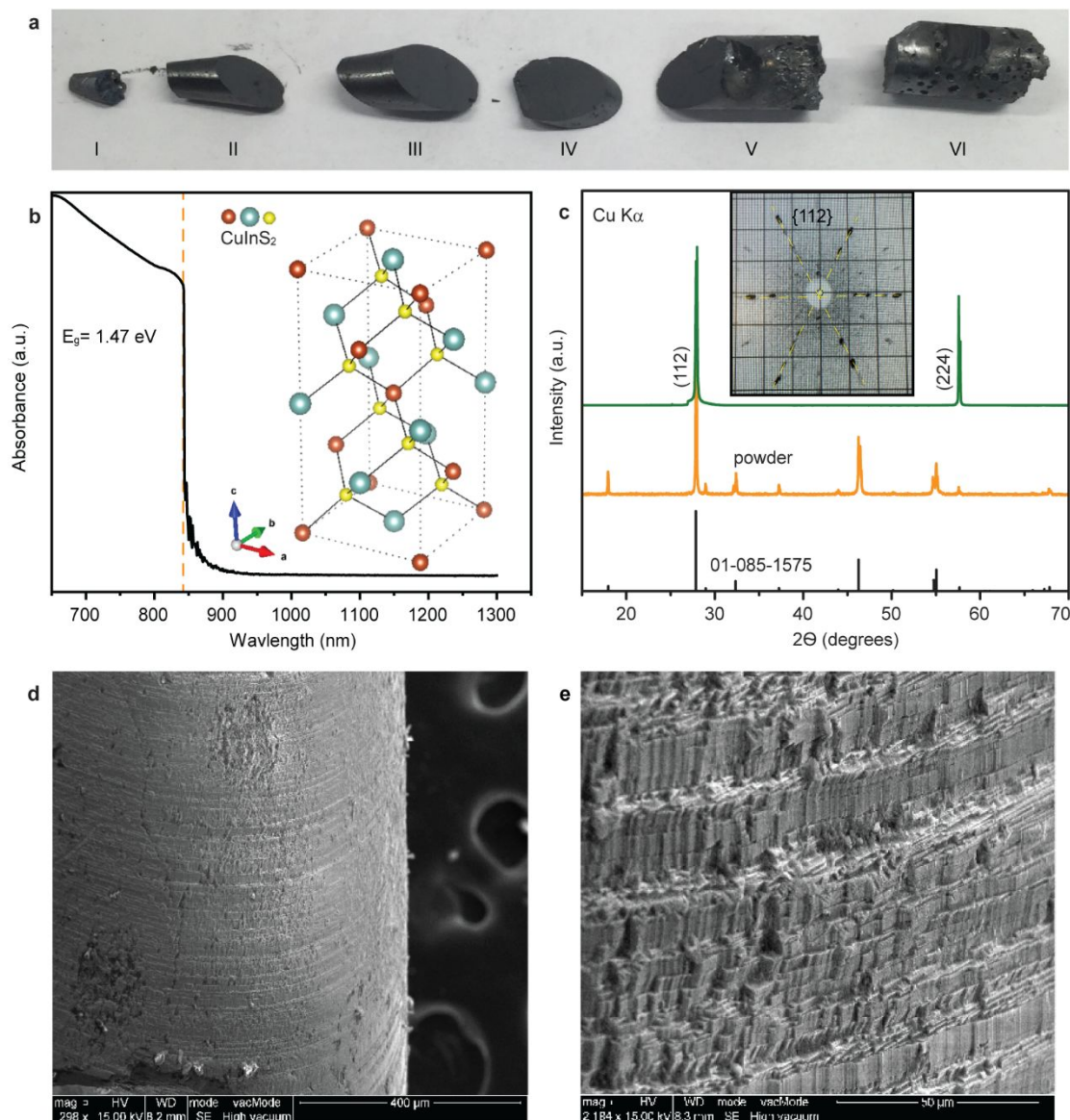


**Figure 1. Structural and optical characterization of 1 mol% Cu-deficient  $\text{CuInS}_2$  single crystal.** **a**, The single crystal boule cleaved along the (112) in six sections upon extraction from the growth ampoule. All measurements in this work were performed on crystals extracted from section IV. **b**, Optical absorption spectrum of  $\text{CuInS}_2$ , showing a sharp onset of absorption at 1.47 eV. A freshly cleaved (112) slab (0.3 mm thick) was exposed for this measurement. The inset shows the tetragonal chalcopyrite structure of  $\text{CuInS}_2$ . **c**, XRD pattern of the single crystal face (green), powder form (orange), and database pattern match (black). The inset shows a Laue diffraction pattern of the (112) crystal surface. SEM imaging of section IV is presented at magnification **d**, 250x and, **e**, 2000x, revealing the pronounced (112) terraces on the perimeter of the crystal boule.

**3.2 Microstructure of the bulk chalcopyrite  $\text{CuInS}_2$ .** Samples for transmission electron microscopy were prepared by focused ion beam cutting in a FEI Helios NanoLab™ 600 dual beam system (FIB/SEM). Conventional TEM imaging, atomic resolution high-angle annular dark-field (HAADF) scanning transmission electron microscopy (STEM) imaging, and atomic-level EDS

1  
2  
3 mapping were performed on a double Cs-corrected FEI Titan Cubed Themis 300  
4 scanning/transmission Electron Microscope (S/TEM) equipped with an X-FEG source operated at  
5  
6 300 kV and a Super-X EDS system. Relative compositions were determined with EDS by  
7  
8 integrating the area of the elemental peaks. The stated compositions are average values over  
9  
10 selected areas or pixels (making image resolution important); their estimated accuracy is  $\pm 0.5$  at.%.  
11  
12 The TEM elemental signal at a given atom position is produced by a whole column of atoms that  
13  
14 are superposed in the  $\sim 100$  nm thick sample. Therefore, the signal intensity combines the electron  
15  
16 density ( $Z$  number) of the particular atom (or atoms when viewing in directions where Cu and In  
17  
18 are superposed—see Fig. 4c) with the occupation of the column. While the EDS signal does not  
19  
20 directly tell us the number of occupied sites in an atomic column, line scans or area scans do trace  
21  
22 *changes* in occupation, and hence, composition; maximal intensity reflects complete occupation  
23  
24 of a column, as in bulk  $\text{CuInS}_2$ .  
25  
26  
27  
28  
29

30  
31 The TEM image in Figure 2a taken in the  $\langle 1\bar{1}0 \rangle$  direction shows that the  $\text{CuInS}_2$  crystal  
32  
33 has a lamellar structure. The lamellae are alternating pseudo-twins that form a herringbone pattern.  
34  
35 The thickness of the lamellae ranges from several nm to hundreds of nanometers. The  
36  
37 corresponding composite diffraction patterns from the pseudo-twins are shown in the bottom  
38  
39 panels of Fig. 2a. They are taken from the  $\langle 1\bar{1}0 \rangle$  and  $\langle \bar{1}\bar{1}1 \rangle$  zone axes, respectively, and identify  
40  
41 the pseudo-twin plane as  $\{112\}$ . The pseudo twins are separated by a rotational-twin boundary (a  
42  
43  $180^\circ$  rotation)<sup>24</sup> that has been theorized to be the most energetically favored twin boundary in  
44  
45 chalcopyrites, as it avoids the reconstruction that would be inevitable in anion- and cation-  
46  
47 terminated twin boundaries.<sup>51,52</sup> Pairs of twins are imaged at the tops and bottoms of each frame  
48  
49 of Fig. 2b and c.  
50  
51  
52  
53  
54  
55  
56  
57  
58  
59  
60

1  
2  
3 Periodic interfacial structures (“interphases”) are seen to be inserted into the pseudo-twin  
4  
5  
6  
7  
8  
9  
10  
11  
12  
13  
14  
15  
16  
17  
18  
19  
20  
21  
22  
23  
24  
25  
26  
27  
28  
29  
30  
31  
32  
33  
34  
35  
36  
37  
38  
39  
40  
41  
42  
43  
44  
45  
46  
47  
48  
49  
50  
51  
52  
53  
54  
55  
56  
57  
58  
59  
60

boundaries. In Fig. 2b and c these structures are viewed by aberration-corrected scanning transmission electron microscopy (STEM) from the  $\langle 1\bar{1}0 \rangle$  and  $\langle \bar{1}\bar{1}1 \rangle$  directions, respectively. The interphases at the pseudo-twin boundaries, shown schematically in Fig. 2d, contain a single (top frames of Fig. 2b and c) or a double (bottom frames) layer. In Fig. 2c the bulk chalcopyrite exhibits alternating pairs of bright (In stack) and faint (Cu stack) spots. As seen in the top frames, the single-layer interfacial structure includes two bright atomic planes but with interplanar spacings different from those of the chalcopyrite  $\text{CuInS}_2$  bulk. The bulk twins sandwich the interfacial

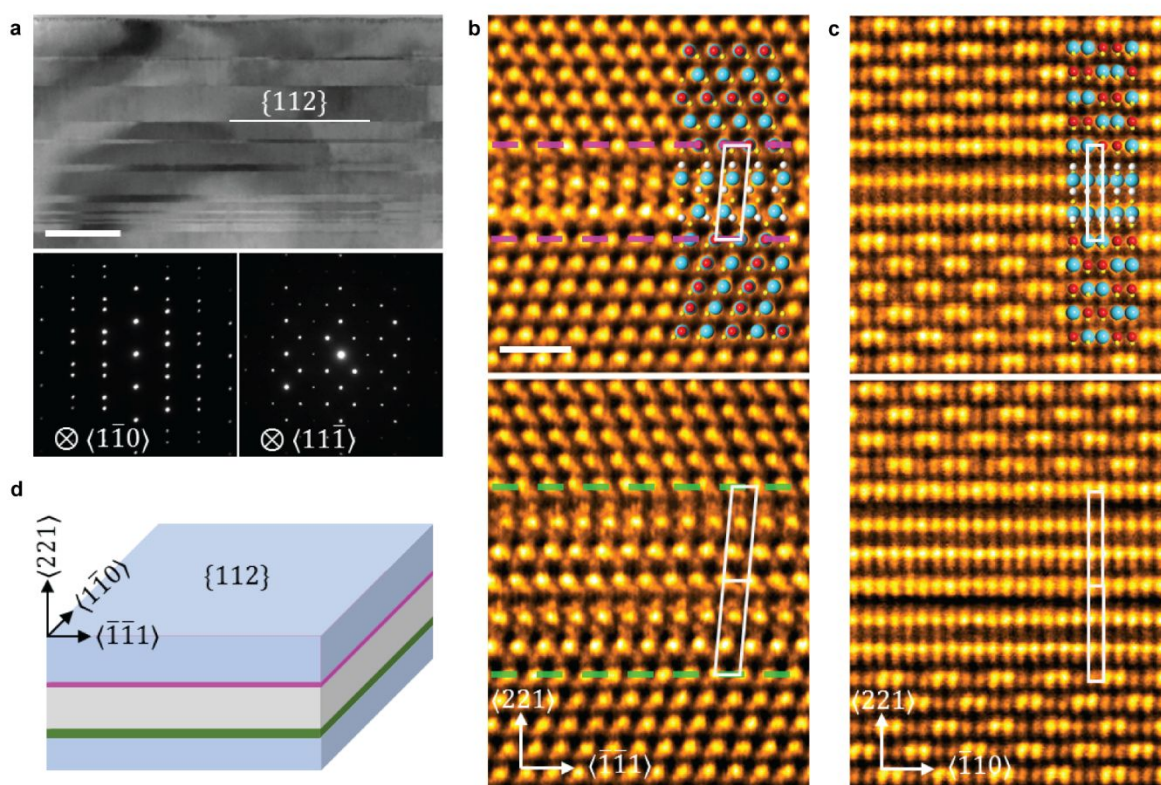


**Figure 2. Microstructure of chalcopyrite  $\text{CuInS}_2$ .** **a**, Bright-field TEM image showing lamellar pseudo-twins. The pseudo-twin plane is  $\{112\}$ . Scale bar, 500 nm. The corresponding composite diffraction patterns of the bottom panels were taken along the  $\langle 1\bar{1}0 \rangle$  and  $\langle \bar{1}\bar{1}1 \rangle$  zone axes, respectively. **b**, **c**, High-resolution STEM HAADF images showing parts of chalcopyrite  $\text{CuInS}_2$  pseudo-twins above and below single (top frames) and double layers (bottom), viewed from the  $\langle 1\bar{1}0 \rangle$  and  $\langle \bar{1}\bar{1}1 \rangle$  directions, respectively. A color-coded chalcopyrite structure (Cu, red; In, blue; S, yellow) is overlaid on the TEM images to identify atoms. In Fig. 2c, atomic-column pairs of Cu and In can be seen—note the alternation of bright (In) and faint (Cu) pairs in the bulk crystal. Scale bar, 1 nm. **d**, Schematic illustration of (blue or gray) bulk  $\text{CuInS}_2$  pseudo-twin lamellae separated by a single (magenta) and a double (green) interphase, all stacked in the  $\langle 221 \rangle$  direction.

phase. Note, again, that in the atomic resolution images, changes in spot size or intensity reflect changes of the type and/or the number of atoms in the stack at that position.

1  
2  
3 **3.3 Composition of bulk crystal and of interfacial structures.** The chemical compositions of  
4 bulk and interphases were determined by mapping the three elements by atomic-level STEM  
5 energy-dispersive X-ray spectroscopy. Figure 3a and b show STEM-HAADF images of bulk  
6 chalcopyrite  $\text{CuInS}_2$ , and the corresponding elemental maps of Cu (red), In (green), and S (blue),  
7 viewed along the  $\langle 1\bar{1}0 \rangle$  and  $\langle \bar{1}\bar{1}1 \rangle$  directions, respectively (see more details of single-element  
8 mappings in the SI, Fig. S2). The bulk composition is 25.2 at.% Cu, 24.3 at.% In and 50.5 at.% S,  
9 (SI, Table S1), which is, within accuracy, the stoichiometry of  $\text{CuInS}_2$ . The chalcopyrite unit cell  
10 is delineated to identify the atomic positions. While in the  $\langle 1\bar{1}0 \rangle$  projection (Figs. 3a and 4c) Cu  
11 and In atoms lie on top of each other, in the  $\langle \bar{1}\bar{1}1 \rangle$  projection of Fig. 3b they alternate (bright, In;  
12 weak, Cu).  
13  
14  
15  
16  
17  
18  
19  
20  
21  
22  
23  
24  
25

26 We used EDS to also determine by how much the composition of the interphases deviates  
27 from bulk  $\text{CuInS}_2$ , along the trace marked in the HAADF image of Fig. 3c. The panel at its right  
28 shows the element maps of Cu (red), In (green) and S (blue). The lower left panel shows the EDS-  
29 determined concentration profiles along the trace in the STEM-HAADF image above. With respect  
30 to the bulk, the interfacial layers are depleted of Cu (down -7.9 at.% in the single layer and down  
31 -11.5 at.% in the double layer) and contain up to +8.6 at.% excess In and +3.0 at.% excess S. Thus,  
32 while the bulk contains 25.2 at.% Cu, the single and double interfacial phase layers contain only  
33 17.1 at.% and 13.7 at.% Cu, respectively, but 32.9 at.% In (for sulfur see SI, Table S1). An  
34 additional example, analyzed along the  $\langle \bar{1}\bar{1}1 \rangle$  direction, is provided in the SI, Fig. S3. The copper  
35 deficiency of the interfacial phase suggests that the interfacial phase accommodates the copper  
36 deficiency of the overall crystal.  
37  
38  
39  
40  
41  
42  
43  
44  
45  
46  
47  
48  
49  
50

51 **3.4 Structure of the Cu-deficient interphases, and the  $[V_{\text{Cu}} \text{In}_i V_{\text{Cu}}]$  triple point defect.** The  
52 atomic occupations in the interfacial structures can be deduced from the atomic resolution STEM-  
53  
54  
55  
56  
57  
58  
59  
60

HAADF images of Fig. 2b and c. Figure 4 shows the corresponding atomic models of a single-layer interfacial structure (top frames of Fig. 2b and c), viewed from  $\langle 1\bar{1}0 \rangle$  and  $\langle \bar{1}\bar{1}1 \rangle$ , respectively.

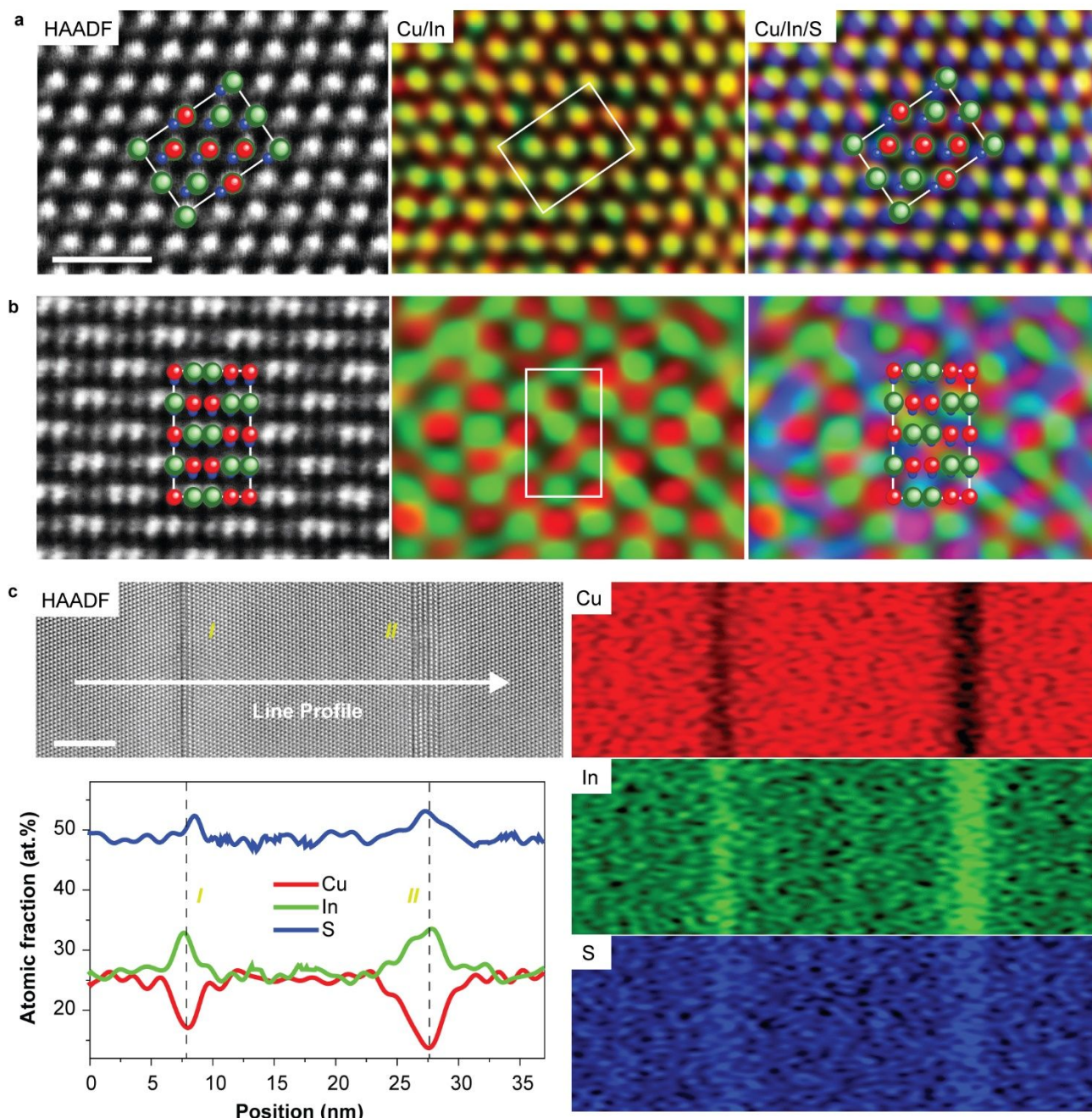


**Figure 3. Quantitative analysis of composition.** **a,b**, Atomic-level STEM-EDS maps showing the positions of Cu (red), In (green) and S (blue) in bulk chalcopyrite CuInS<sub>2</sub>. The top row is viewed along the  $\langle 1\bar{1}0 \rangle$  direction and the second row along  $\langle \bar{1}\bar{1}1 \rangle$ . The leftmost panels show HAADF-STEM images, the center panels the element mappings of Cu/In and the right panels of Cu/In/S. The chalcopyrite unit cell is delineated to highlight the positions of the three elements. In the  $\langle 1\bar{1}0 \rangle$  projection Cu and In atoms are superposed; in the  $\langle \bar{1}\bar{1}1 \rangle$  projection they are separate. Scale bar, 1 nm. **c**, STEM-EDS mapping of bulk CuInS<sub>2</sub> including one pseudo-twin boundaries with a single (I) and one with a double (II) interphase layer. The HAADF image shows the EDS trace across the bulk and the two interphases. The right panel combines the elemental maps of Cu (red), In (green) and S (blue) from multiple scans. The compositional profiles along a single scan, at bottom left, show Cu depletion and In and S enrichment in the interfacial layers. Scale bar, 5 nm. To improve the contrast in elemental maps, color coding in this Figure, and in Figs. S2 and S3, is red/green/blue, different from the red/blue/yellow in Figs. 1, 2, 4, and 5.



Note the color codes in Figs. 4 and 5, where In is coded blue and S yellow throughout; the Cu position, however, is coded red in the chalcopyrite structure but gray in the interphase, the latter because we cannot exclude partial occupation by In. In Fig. 4a, viewed along the  $\langle 1\bar{1}0 \rangle$  direction, Cu and In overlap in the chalcopyrite bulk structure, as further illustrated in the unit cell of Fig. 4c. Viewed along  $\langle \bar{1}\bar{1}1 \rangle$  in Fig. 4b, the Cu and In positions are separate. The black quadrangles in Fig. 4a and b delineate the minimal cells of the interphase structures.

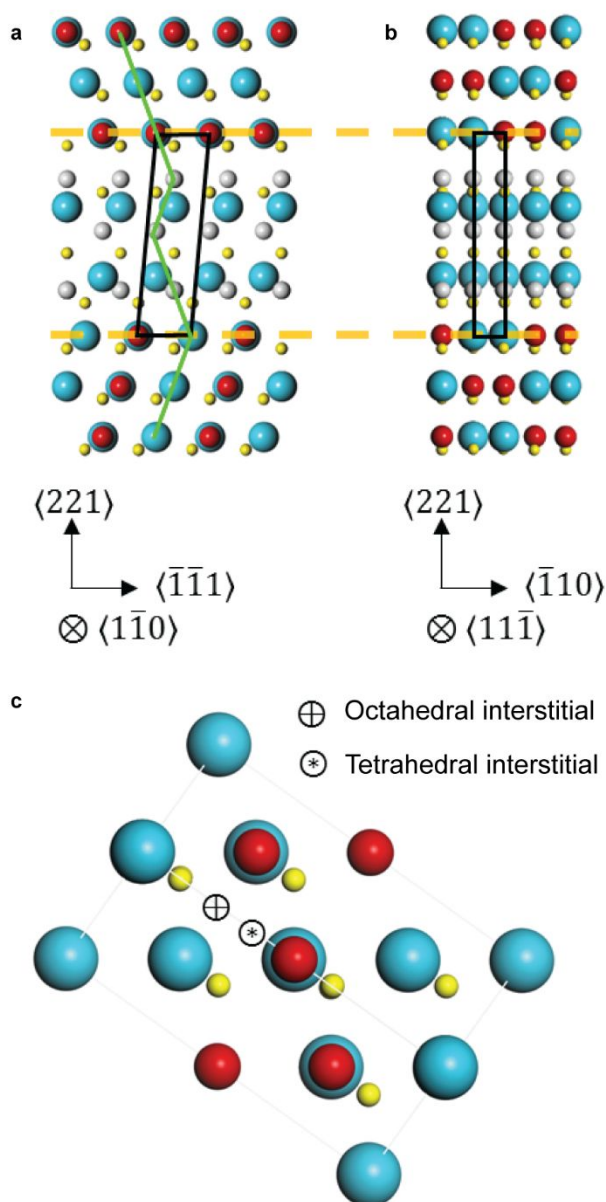


**Figure 4. Schematic of the interfacial structure.** **a, b,** Atomic model of the single-layer interfacial structure (top frames of Fig. 2b and c) viewed along the  $\langle 1\bar{1}0 \rangle$  and  $\langle \bar{1}\bar{1}1 \rangle$  zone axes, respectively. **c,** Chalcopyrite unit cell viewed in the  $\langle \bar{1}\bar{1}0 \rangle$  direction, identifying the interstitial sites. Note the overlaid Cu (red) and In (blue) positions. The ball size qualitatively reflects the  $Z$  (= electron) number of a given atom.

1  
2  
3  
4  
5  
6  
7  
8  
9  
10  
11  
12  
13  
14  
15  
16  
17  
18  
19  
20  
21  
22  
23  
24  
25  
26  
27  
28  
29  
30  
31  
32  
33  
34  
35  
36  
37  
38  
39  
40  
41  
42  
43  
44  
45  
46  
47  
48  
49  
50  
51  
52  
53  
54  
55  
56  
57  
58  
59  
60

Because the atom positions in the interphases are largely derived from those in the bulk, we turn to inspecting the STEM-HAADF image of Fig. 5 taken along the  $\langle 1\bar{1}0 \rangle$  zone axis (see Fig. 4a). Figure 5 shows a transition from a pseudo-twin boundary in the bulk, at left, to a single-layer interphase. Three In rows of the chalcopyrite bulk are seen to merge into two rows (blue) in the interphase. There, one row lies at the normally occupied chalcopyrite site  $\text{In}_{\text{In}}$  (e.g.,  $1/4, 1/4, 1/8$ ). The other row of In is positioned as interstitial  $\text{In}_i$  at tetrahedral interstices (e.g.,  $3/4, 1/4, 1/8$ ) in the chalcopyrite structure, identified in Fig. 4c. The additional occupation of tetrahedral sites forms an In-enriched interfacial layer. While in the transition from bulk to interphase the Cu atoms remain in their bulk  $\text{Cu}_{\text{Cu}}$  positions, Fig. 5a shows that their intensity fades in the transition from left to right. To remind the reader that in the interphase these positions remain normal Cu-on-In stacks (instead of Cu only) they are color-coded gray. However, their intensity becomes so small that we can be certain that in going from bulk to interphase many  $\text{Cu}_{\text{Cu}}$  sites in the stack are emptying out and become copper vacancies,  $\text{V}_{\text{Cu}}$ . Note that, as Cu fades, the In intensity increases going from left to right, a consequence of the merger of three rows in the bulk to two rows in the interphase. Thus, a dominant feature of the interphase is a fully occupied In stack (blue) placed between two stacks that, given their faint intensity, are highly deficient in Cu (gray). In the interphase, the EDS concentrations of Fig. 3c go down to a Cu deficiency of 11.5 at.% and up to an In excess of 8.6 at.%. Hence, the estimated atomic ratio of  $\text{V}_{\text{Cu}}$  to  $\text{In}_i$  is  $11.5/8.6 = 1.34$ . Taken together, the atomic positions of two faint Cu stacks sandwiching the  $\text{In}_i$  stack, plus this ratio 1.34, are structural and compositional indicators for a high concentration of  $[\text{V}_{\text{Cu}} \text{In}_i \text{V}_{\text{Cu}}]$  defect triplets.  $\text{In}_{\text{In}}$  is an electron donor, and  $\text{V}_{\text{Cu}}$  is an electron acceptor. The defects will exchange charge, such that  $[\text{V}_{\text{Cu}} \text{In}_i \text{V}_{\text{Cu}}]$  triplets self-compensate to electrically neutral  $[\text{V}_{\text{Cu}}^{1-} \text{In}_i^{2+} \text{V}_{\text{Cu}}^{1-}]$ .

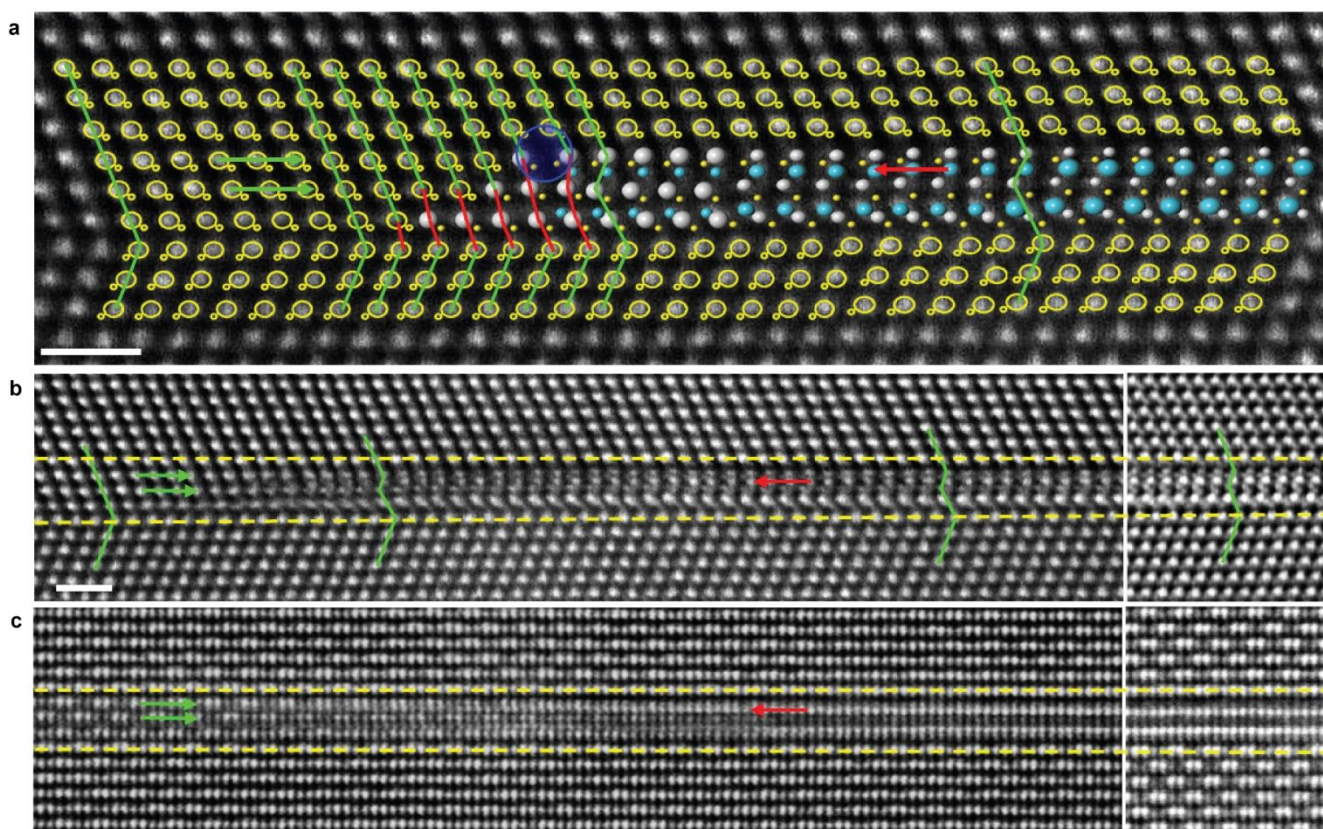


**Figure 5. Transition from pseudo-twin boundary to interphase, observed going from left to right.** **a**, Magnified STEM-HAADF image along the  $\langle 1\bar{1}0 \rangle$  zone axis, with an overlaid atomic model to highlight the interfacial defect formed by the pseudo-twin boundary. The big and small open circles in the  $\text{CuInS}_2$  bulk structure represent the occupations of Cu/In and S, respectively (see Fig. 2b). The In (blue) and S (yellow) atoms located in the interphase layer are color coded as in Figs. 1a, 2b, c, and 4. Cu is shown in grey (see text). The chalcopyrite phase at left has In and Cu atoms that lie on top of each other in their normal positions (grey). Going to the right, one can see that In (blue) has emerged from that stack by moving to a new position, which is the tetrahedral interstitial site of chalcopyrite. **b**, **c**, Original STEM-HAADF images, viewed along the  $\langle 1\bar{1}0 \rangle$  and  $\langle \bar{1}\bar{1}1 \rangle$  zone axes, showing how the interphase emerges from the pseudo-twin boundary. Sectioned off at right are images taken far from this transition. Scale bars, 1 nm.

The crystal contains planar, line and point defects. The interphase introduces a defect plane.

This plane becomes apparent when counting from the meeting point of the herringbone pseudo-twin lattice planes in the bulk (green lines with elbows at the left of Fig. 5a and b) to equivalent planes separated by the interphase. There the equivalent bulk planes are offset, as illustrated in Fig. 5a and b (and Fig. 4a) by the jogs in the green lines that run from bulk to bulk across the interphase. This slip plane constitutes a planar defect that is contained in the interphase.

1  
2  
3 The transition from or to the pseudo-twin plane to interphase produces a line defect, which  
4 in Fig. 5a is surrounded by the blue circle. This is a partial dislocation,  $1/6 \langle \bar{1}\bar{1}1 \rangle$ , which is similar  
5 to the  $1/6 \langle 112 \rangle$  in the face-centered cubic system. This dislocation compensates the displacement  
6 of interfacial atoms that is traced by the red lines. The blue circle around the positions of the atoms  
7 that surround the dislocation draws attention to the mispairing of coordinative bonds caused by the  
8 change of atomic stacking. As seen in the SI, Fig. S4, some of the interlayer phases form disks that  
9 are fully embedded in the crystal (instead of running from side to side), and therefore will be  
10 surrounded by a ring of these partial dislocations.

11  
12 Thus, structural defects include the (112) pseudo-twin boundary of the bulk crystal, the  
13 (112) slip plane within the interphase, the  $1/6 \langle \bar{1}\bar{1}1 \rangle$  partial dislocation at the perimeter of the  
14 interphase, as well as  $\text{In}_i$  and  $\text{V}_{\text{Cu}}$  within the interphases. What are their opto-electronic  
15 consequences?

16  
17 **3.5 Electronic transport and photoconductivity.** Electronic transport properties were  
18 measured along the (112) plane of an  $2 \times 3 \times 0.3 \text{ mm}^3$  sample with eutectic In-Ga contacts made on  
19 the (112) surface and Pt lead wires, using a Quantum Design Physical Property Measurement  
20 System (PPMS). In-plane resistivity vs. temperature data (plotted in Fig. 6) was collected from  
21 395 K to 300 K—where we reached the measurement limit of our equipment. At  $T = 300 \text{ K}$ ,  $\rho_{xx}$  is  
22  $2.7 \times 10^6 \Omega \cdot \text{cm}$ . From plotting  $\log(\rho_{xx})$  vs.  $1/T$  (inset, Fig. 6a) we extract the thermal activation  
23 energy of 87 meV. Hall effect measurements performed at magnetic fields from  $\mu_0 H = -3$  to 3 T at  
24 300 K gave the Hall resistivity  $\rho_{xy}$ , shown in Fig. 6b. The actual quantity plotted is  $\rho_{xy}$  with some  
25 admixture of  $\rho_{xx}$  because the Hall contacts were not made exactly orthogonal to the current and  
26 field directions. The negative slope reflects  $n$ -type conduction. The calculated electron  
27 concentration,  $n$ , is  $2.3 \times 10^{13} \text{ cm}^{-3}$ , and the electron mobility,  $\mu_n$ , calculated from  $\rho_{xy}$  and  $n$ , is 0.1

cm<sup>2</sup> V<sup>-1</sup> s<sup>-1</sup>. While high  $\rho$  and low  $n$  have been observed before,  $\mu_n$  is unusually low.<sup>6,9</sup> Given that the (112) interphase layers embedded in the crystal may cause anisotropic conduction, we made a

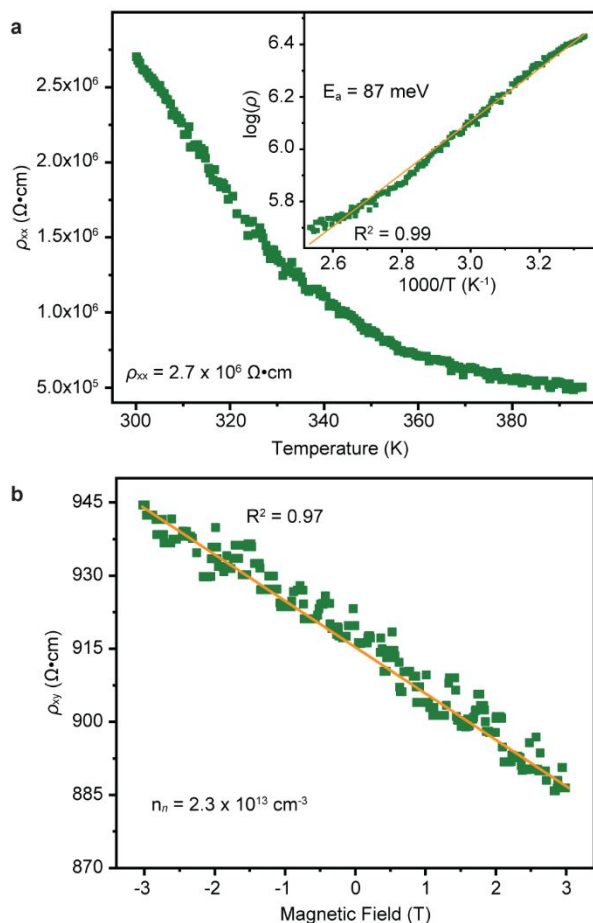


**Figure 6. Electrical characterization of the 1 mol% Cu-deficient CuInS<sub>2</sub> single crystal. a,** Resistivity ( $\rho_{xx}$ ) vs. temperature profile from 300-395 K. The inset plots this data as  $\log \rho_{xx}$  vs.  $1/T$  from which an activation energy of 87 meV is extracted. **b,** Hall resistivity ( $\rho_{xy}$ ) vs. magnetic field from  $\mu_0 H = -3$  to 3 T at 300 K. The negative slope identifies electrons as the crystal's majority carrier. From this data we can calculate an electron concentration,  $n$ , of  $2.3 \times 10^{13} \text{ cm}^{-3}$ .

top-to-bottom ([112] direction) resistance measurement, from which we estimate  $\rho_{zz} \approx 1 \times 10^6 \Omega \cdot \text{cm}$ , i.e., close to the  $\rho_{xx}$  measured laterally.

Photoconductivity was measured in the configuration shown in the inset to Fig. 7a, with InGa eutectic and Pt wire contacts applied to the (112) face of the sample that had been characterized by TEM. LEDs of the eight different wavelengths (ThorLabs, FWHM  $\approx 55$  nm) shown in Fig. 7a illuminated the sample at irradiances ranging from 0.25 to 70 mW/cm<sup>2</sup>, over voltages from +/- 10 V supplied by the PPMS. Illumination with LEDs enables high irradiance, at the expense of modest spectral resolution. Irradiances were measured using a digital handheld

optical power meter (model PM100D, Thorlabs) coupled with a Photodiode Power Sensor (model S120VC, Thorlabs).

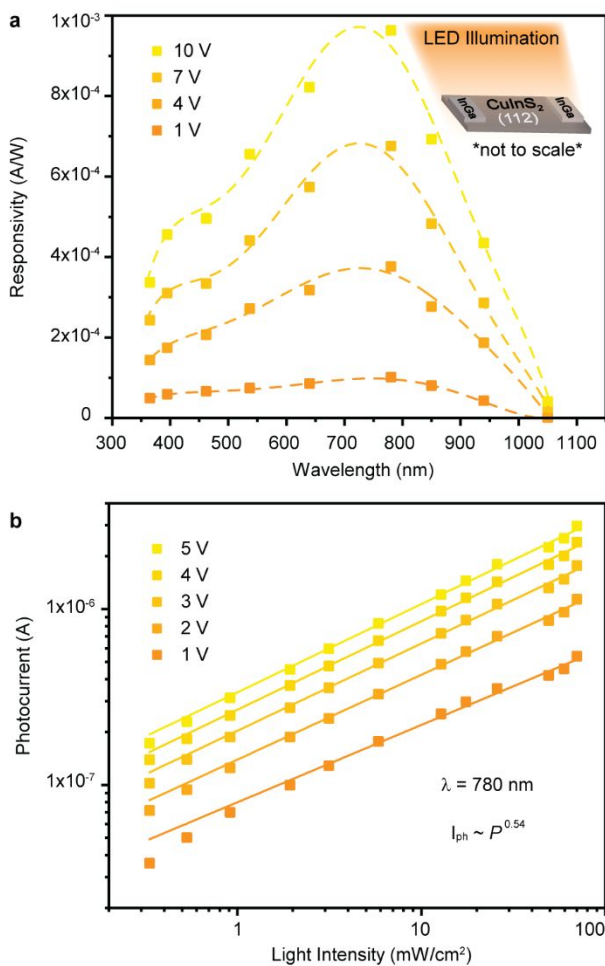


**Figure 7. The photo-electric properties of the  $\text{CuInS}_2$  crystal.** **a**, Responsivity vs. wavelength for four applied voltages. Responsivity is highest at 780 nm. The inset shows the measurement geometry. **b**, Photocurrent vs. light intensity at 780 nm illumination for five applied voltages. A simple power law fit (solid lines) results in an exponent of 0.54.

In the responsivity vs. wavelength graph of Fig. 7a, for applied voltages ranging from 1 V to 10 V, dotted lines serve as guides for the eye. The responsivity peaks at 780 nm, corresponding to a photon energy of 1.59 eV ( $\pm 0.05$  eV LED FWHM). The linear decrease in responsivity with wavelengths below 780 nm reflects a constant quantum efficiency. While SI, Fig. S5 shows the photocurrent vs. voltage plot for 780 nm irradiance from 0.25 to 70  $\text{mW}/\text{cm}^2$ , Fig. 7b shows the log-log plot of the photocurrent vs. 780 nm irradiance. The dependence of log photocurrent on log light intensity is linear and fits a simple power law:  $I_{ph} = AP^\alpha$  where  $I_{ph}$  is the photocurrent,  $A$  is a

1  
2  
3 scaling constant,  $P$  is the irradiance, and  $\alpha$  is an exponent. The solid lines represent this fit. The  
4  
5 slopes of these fits for 2V to 5V applied bias are identical at  $\alpha = 0.54$ .<sup>53</sup>  
6  
7

#### 8 4. DISCUSSION

9  
10 **4.1 The  $[V_{Cu} In_i V_{Cu}]$  triple point defect.** Electron microscopy of structure and composition at  
11  
12 atomic resolution shows that introducing Cu deficiency in a  $CuInS_2$  crystal results in exactly  
13  
14 stoichiometric  $CuInS_2$  bulk with intercalated sheets of a phase that is highly Cu deficient and In  
15  
16 rich. These interphases lie in (112) planes, are nanometers thick, and contain either two or four In  
17  
18 layers. Analysis of the transition from chalcopyrite-type bulk  $CuInS_2$  to the interphase shows that  
19  
20 three (or six)  $In_m$ -containing layers from normal sites in the bulk merge to two (or four) layers of  
21  
22 interstitial  $In_i$  in the interphase, while the positions and number of the three (or six) corresponding  
23  
24 Cu and S containing layers are preserved in the transition from bulk to interphase. There, the  
25  
26 positions of  $Cu_{Cu}$  (and therefore  $V_{Cu}$ ) on normal sites bracket interstitial  $In_i$  atoms. While the  
27  
28 atomic positions in Fig. 5 do not reveal the actual occupation of sites within each stack, Coulombic  
29  
30 attraction will make two  $V_{Cu}^{1-}$  become nearest neighbors of one  $In_i^{2+}$ . This positioning, the  
31  
32 estimated  $Cu_{Cu}$ ,  $V_{Cu}$  and  $In_i$  concentrations, and the high electrical resistivity of the sample taken  
33  
34 together are conclusive indicators for the existence of electrically neutral  $[V_{Cu}^{1-} In_i^{2+} V_{Cu}^{1-}]$   
35  
36 triplets.<sup>45</sup> These are the basic structural modifier of ordered defect compounds in I-III-IV diamond-  
37  
38 like semiconductors. The pronounced separation into stoichiometric  $CuInS_2$  and a highly Cu-  
39  
40 deficient interlayer phase confirms that the Cu deficient phase has high thermodynamic stability  
41  
42 with respect to bulk  $CuInS_2$ . The cause of this stability is the reduction of Cu content, which  
43  
44 diminishes the intensity of repulsion by the antibonding Cu  $d - S p$  hybrid states that form the top  
45  
46 of the valence band.  
47  
48  
49  
50  
51  
52  
53  
54  
55  
56  
57  
58  
59  
60

1  
2  
3 A rough estimate suggests that the interphase layers absorb much of the Cu deficiency  
4 introduced with the initially Cu-deficient charge used for crystal growth. Viewing the excess In in  
5 the interphases as the binding agent for Cu vacancies that have diffused out from the bulk  $\text{CuInS}_2$ ,  
6 we calculate the concentration of  $V_{\text{Cu}}$  as approximately twice that of excess indium. EDS measures  
7 that the interphase with two rows of indium contains 8.6 at.% excess indium. This corresponds to  
8  $(2 \text{ rows}) \times (2 V_{\text{Cu}} \text{ per In}_i) \times 8.6 \text{ at.\% excess In}_i \cong 34 \text{ at.\% of Cu missing from that interphase}$ . The  
9 interphase accommodates three rows of copper, just like the bulk. Therefore, the overall Cu  
10 deficiency in the interphase is  $3 \times 34 \text{ at.\%} = 102 \text{ at.\%}$ , equivalent to about one row of  $V_{\text{Cu}}$ . The  
11 average thickness of bulk  $\text{CuInS}_2$  between the interphase layers is  $\sim 100 \text{ nm}$ , which corresponds  
12 to  $\sim 300$  layers of atoms. Following this argument, the original fraction of Cu vacancies in the  
13 hypothetical homogeneous, non-stoichiometric, crystal would have been  $\sim 1/300 \cong 0.003$ , a value  
14 close to the targeted Cu deficiency of 1 mol% [ $0.25 - 0.003 = 0.247 \text{ at.\%}$ ] of the starting material.  
15 This approximate agreement suggests that excess  $\text{In}_i$  is a titer for  $V_{\text{Cu}}$ , and that the interphases  
16 efficiently soak up  $V_{\text{Cu}}$  where they are thermodynamically quite stable.

17  
18 Under the electron beam, the edge of an embedded interphase can be moved back and forth  
19 like a zipper. That observation implies fast movement of atoms. When zipping to extend the  
20 interphase, two rows of  $\text{In}_i$  can revert to three rows of  $\text{In}_{\text{In}}$  with minimal atomic displacement. S  
21 stays in its normal sites, as does Cu. However, a newly extended perimeter of the interphase needs  
22 stabilization by Cu vacancies. The observed zipper-like fluidity implies that  $V_{\text{Cu}}$  are supplied  
23 rapidly from the depth of the interphase to its growing edge. The electron beam likely provides the  
24 energy needed to dissociate the  $[V_{\text{Cu}}^{1-} \text{In}_i^{2+} V_{\text{Cu}}^{1-}]$  triplets, thereby supplying  $V_{\text{Cu}}$  to the advancing  
25 edge. Because of the high  $V_{\text{Cu}}$  concentration,  $\text{Cu}_{\text{Cu}}$  atoms will move easily between the Cu sites,  
26  
27  
28  
29  
30  
31  
32  
33  
34  
35  
36  
37  
38  
39  
40  
41  
42  
43  
44  
45  
46  
47  
48  
49  
50  
51  
52  
53  
54  
55  
56  
57  
58  
59  
60



perhaps even functioning as a (112) confined sheet of  $\text{Cu}_{\text{Cu}}$  ‘liquid’. Similarly, illumination has been observed to render  $[\text{V}_{\text{Cu}}^{1-} \text{In}_{\text{Cu}}^{2+} \text{V}_{\text{Cu}}^{1-}]$  triplets in  $\text{CuInSe}_2$  nanocrystals high mobile.<sup>54</sup>

**4.2 Crystallographic defects.** While the existence of the  $[\text{V}_{\text{Cu}}^{1-} \text{In}_{\text{Cu}}^{2+} \text{V}_{\text{Cu}}^{1-}]$  triplet is made certain by a group of observations that prove the existence of a high concentration of  $\text{V}_{\text{Cu}}$  at the appropriate positions in the interphases, several crystallographic defects can be seen directly. They include the pseudo-twin boundary in the (112) planes, separating lamellae of  $\text{CuInS}_2$  that are rotated  $180^\circ$  against their neighbors;  $1/6 \langle \bar{1}\bar{1}1 \rangle$  partial dislocations that accommodate a bond mismatch at the periphery of the embedded interphase layers, and a one-bond offset with respect to the bulk, of lattice planes that terminate at interphase layers. Typically, such planar and line defects cause electronic defects, and indeed many point defects have been postulated for  $\text{CuInS}_2$ .<sup>45,55–61</sup> While no specific electronic defect has been identified in the present study, the observed photoconductivity exponent of 0.54 suggests that electronic defect levels do exist in the energy band gap, with a density of defect states decaying away from the band edges.<sup>53,62</sup> For a comprehensive overview of point defects in a chalcopyrite, the reader is referred to the discussion of  $\text{CuInSe}_2$  by Zhang et al.<sup>45</sup>

The fully embedded interphase (SI, Fig. S4) demonstrates that pseudo-twin boundaries do exist in the absence of interphases. This suggests that at least some, and possibly all, of the interphases did form following the growth of a non-stoichiometric crystal. While Fig. 5 shows that the excess In in the interphases can be supplied by the merger of three In layers in bulk  $\text{CuInS}_2$  to two layers in the interphase,  $\text{V}_{\text{Cu}}$ , however, must collect in the interphase by diffusion from the surrounding bulk. Figure 2a shows that the pseudo-twin boundaries, where the interphases are located, are spaced  $\sim 100$  nm apart. It is instructive to compare the diffusion lengths of Cu and In under the crystal’s annealing conditions of  $400^\circ\text{C}$  for 24 hours, because that is the lowest

1  
2  
3 temperature at which a solid-state reaction might have proceeded in the present crystal. The  
4  
5 diffusion coefficient of  $\text{Cu}^{1+}$ , determined from NMR line narrowing,<sup>63</sup> is  $D(\text{Cu}^{1+}) = 5 \times 10^{-3} \times \exp(-$   
6  
7  $1.25 \text{ eV} / kT) \cong 2 \times 10^{-12} \text{ cm}^2\text{s}^{-1}$  at 400 °C. The diffusion coefficient of In, determined with a  
8  
9 radioactive tracer experiment at 650 °C, is  $D(\text{In}) = 8.0 \times 10^{-10} \text{ cm}^2\text{s}^{-1}$ ;<sup>50</sup> the thermal activation energy  
10  
11 was not measured. At 650 °C the calculated diffusion coefficient of Cu =  $7 \times 10^{-10} \text{ cm}^2\text{s}^{-1}$  is  
12  
13 essentially the same as that of In, surprisingly, given that Cu is considered to be less strongly bound  
14  
15 in the chalcopyrite than In. Assuming the same activation energies for Cu and In diffusion, at 400  
16  
17 °C both diffusion coefficients,  $D$ , will be  $\sim 2 \times 10^{-12} \text{ cm}^2\text{s}^{-1}$ . For a 24-hours long diffusion time,  $t$ ,  
18  
19 the diffusion length  $\sqrt{Dt}$  will be 4  $\mu\text{m}$ , far longer than the  $\sim 100\text{-nm}$  spacing of the Cu poor  
20  
21 interphases. Therefore, as far as Cu and In atomic and associated defect distributions are  
22  
23 concerned, the crystal is equilibrated at 400 °C. While at high temperature the crystal may be  
24  
25 homogeneous single-phase  $\text{CuInS}_2$  with a high concentration of  $V_{\text{Cu}}$ , upon cooling it will segregate  
26  
27 out  $V_{\text{Cu}}$  to interphases at temperatures down to 400 °C.  
28  
29  
30  
31  
32

33 In the present case the Cu-poor interphases form along the (112) pseudo-twin boundary.  
34  
35 Free surfaces of  $\text{CuInS}_2$  can also become Cu poor.<sup>44,64</sup> At grain boundaries, to explain the  
36  
37 passivation to recombination of photo-excited holes in polycrystalline thin film  $\text{CuInSe}_2$  solar  
38  
39 cells, Jaffe and Zunger argue that Cu depletion at grain boundaries sets up an electric field that  
40  
41 repels holes.<sup>65</sup> Similar to this Cu depletion from free surfaces, grain boundaries and device  
42  
43 interfaces,<sup>10</sup> the (112) pseudo-twin boundaries of the present crystal may function as nucleation  
44  
45 sites for the Cu-poor interphases.  
46  
47  
48

49 With the diffusion lengths of Cu and In being much larger than the spacing between the  
50  
51 interphase layers, one may expect some interphases to grow at the expense of others due to Ostwald  
52  
53 ripening. This might have occurred in the present crystal, because only single-thickness  
54  
55  
56  
57  
58  
59  
60

1  
2  
3 interphases are found fully surrounded by bulk  $\text{CuInS}_2$ ; these may be the first stage of  $V_{\text{Cu}}$   
4 segregation. Single-thickness layers that extend through the entire crystal, and even more so,  
5 double layers, may already have benefitted from Ostwald ripening. The observations by Cattarin  
6 and Guerriero suggest that ripening may continue under appropriate crystal growth conditions.<sup>25</sup>  
7  
8 The peculiar structural aspect of a filamentary  $\text{CuInS}_2$  bulk observed by Cattarin et al.<sup>26</sup> was not  
9  
10 seen in the present crystal.  
11  
12  
13  
14  
15

16  
17 **4.3 Optical band gap.** The optical gap determined from the transmission spectrum of 1.47  
18 eV disagrees with the accepted band gap value for  $\text{CuInS}_2$  of 1.53 eV.<sup>8,9,28,66,67</sup> It lies close to the  
19 1.48–1.50 eV optical gaps reported by Cattarin et al.<sup>40</sup> in their work with photoanodes made of  
20  $\text{CuInS}_2$  that had filamentary morphology. The optical gap of 1.47 eV must originate in the  
21 interphase layers. As these occupy  $\sim 1\%$  of the thickness of the 0.3 mm thick sample, the sum of  
22 their thicknesses is  $\sim 3 \mu\text{m}$ . If the joint valence band (VB) – conduction band (CB) states in the  
23 interphase layers remain localized on the Cu atoms,<sup>66</sup> they will absorb light as strongly as bulk  
24  $\text{CuInS}_2$  does. Then the reduction of the Cu concentration to  $\sim 2/3$  of that in bulk  $\text{CuInS}_2$  will reduce  
25 the strength of optical absorption in the interphase by only  $1/3$  from that of  $\text{CuInS}_2$ .  
26  
27  
28  
29  
30  
31  
32  
33  
34  
35  
36

37  
38 Analyses and computations highlight that the valence band maxima (VBM) in  
39 chalcopyrites lie at much higher electron energy (lower ionization energy) than in the equivalent  
40 II-VI semiconductors.<sup>8,45,46,66</sup> The antibonding Cu  $d - X p$  hybrid states in the valence band are the  
41 cause. Reducing the copper content reduces the antibonding repulsion, hence lowers the energy of  
42 the VBM. The conduction band minimum (CBM) is similarly displaced, but usually less strongly  
43 because of the compensating Coulombic attraction between the  $2 V_{\text{Cu}}^{1-}$  and  $\text{In}_{\text{Cu}}^{2+}$  defects. Thus,  
44 band structure calculations suggest that the band gap will increase as the Cu content is reduced.<sup>65</sup>  
45  
46  
47  
48  
49  
50  
51  
52  
53  
54  
55  
56  
57  
58  
59  
60

1  
2  
3 Given the absence of experimental data for  $\text{CuInS}_2$  that verify these theoretical predictions,  
4 we resort to relevant observations in its  $\text{CuInSe}_2$  homolog. Experiments along the  $\text{Cu}_2\text{Se} - \text{In}_2\text{Se}_3$   
5 quasi-binary indeed agree with theory,<sup>68</sup> in that reducing Cu raises the bandgaps of Cu-In-Se  
6 compounds, from chalcopyrite  $\text{CuInSe}_2$  (Cu:In = 1.00) at 0.99 eV, to  $\text{CuIn}_3\text{Se}_5$  (Cu:In = 0.33) at  
7 1.17 eV, to  $\text{CuIn}_5\text{Se}_8$  (Cu:In = 0.20) at  $\sim 1.23$  eV. As well, the corresponding electron affinities  
8 rise from 4.26 eV to 4.48 to  $\sim 4.62$  eV. This rise in bandgap and electron affinity with Cu depletion  
9 was observed in CdS/ $\text{CuInSe}_2$  solar cells.<sup>34</sup> Maeda et al.<sup>68</sup> found that within the  $\text{CuInSe}_2$   
10 homogeneity range, decreasing the Cu concentration does not change the gap, while the gap of the  
11  $\text{CuIn}_3\text{Se}_5$  phase does increase gradually, again, in agreement with theoretical prediction.  
12  
13  
14  
15  
16  
17  
18  
19  
20  
21  
22  
23

24 Returning to the sulfide, Shay, Neumann and Wasim<sup>8,46,66</sup> argue that the sensitivity of the  
25 bandgap value to Cu deficiency will be proportional to the degree of *d-p* hybridization, which is  
26 34% in  $\text{CuInSe}_2$  and 45% in  $\text{CuInS}_2$ .<sup>8</sup> This would mean that the energy positions of the VBM and  
27 the CBM in Cu-In-S compounds will exhibit a more pronounced drop with Cu depletion than of  
28 the Cu-In-Se compounds. In computations, this trend is borne out for the band gaps for  $\text{CuInS}_2$   
29 (1.45 eV) and  $\text{CuIn}_5\text{S}_8$  (1.58 eV), and in the lowering of the CBM energy (i.e., increasing electron  
30 affinity) by 0.50 eV.<sup>37</sup> However, the experimentally measured values for thiospinel-structure  
31  $\text{CuIn}_5\text{S}_8$  do not agree. An indirect gap was detected at 1.29–1.31 eV and a direct gap at 1.51 eV,  
32 both lower than the  $\text{CuInS}_2$  gap of 1.53 eV.<sup>42,43,69</sup> On the other hand, increased open-circuit voltage  
33 in  $\text{CuInS}_2/\text{CdS}$  solar cells is attributed to reduced interface recombination, caused by an increase  
34 of the band gap by Cu depletion.<sup>10</sup> While this observation deserves further analysis, the directly  
35 measured optical absorption edge of the present crystal agrees with neither the theoretical  
36 prediction for a Cu-deficient Cu-In-S phase, nor can it be linked to values observed for  $\text{CuIn}_5\text{S}_8$ .  
37  
38  
39  
40  
41  
42  
43  
44  
45  
46  
47  
48  
49  
50  
51  
52  
53  
54 Likewise, currently available experimental data do not enable verification of the theoretically  
55  
56  
57  
58  
59  
60

1  
2  
3 predicted band edge offsets between CuInS<sub>2</sub> bulk and interphase layers, and further, of their  
4 possible consequences for barriers or quantum wells.<sup>37</sup> As an aside, our observation that the edge  
5 of interphase disks can be moved like a zipper by the electron beam of the microscope suggests  
6 that the coherent strain between bulk and interphase is small, hence may have little effect on band  
7 edge positions.  
8  
9

10  
11 In summary, the observed value of the optical gap of 1.47 eV is ascribed to the Cu-poor  
12 interphase, in disagreement with theoretical predictions for Cu-poor bulk phases. The VBM and  
13 CBM positions of the interphase, and its band edge offsets to CuInS<sub>2</sub> remain to be determined.  
14

15  
16 **4.4 Electronic transport and photoresponse.** The electron mobility of 0.1 cm<sup>2</sup>V<sup>-1</sup>s<sup>-1</sup> is much  
17 lower than literature values, which range from 9 to 338 cm<sup>2</sup>V<sup>-1</sup>s<sup>-1</sup>.<sup>6,9,22,49,55</sup> Only in *p*-type CuInS<sub>2</sub>,  
18 made *p*-type by annealing in sulfur, a similarly low hole mobility of 0.1 cm<sup>2</sup>V<sup>-1</sup>s<sup>-1</sup> has been  
19 reported.<sup>57</sup> Early on, nearly complete donor-acceptor self-compensation was speculated to cause  
20 electron localization, hence low mobility, with the residual donor defects being In<sub>Cu</sub> and V<sub>S</sub>.<sup>55</sup> But  
21 charge carriers are scattered only weakly at highly symmetric grain boundaries like the (112)  
22 pseudo-twin boundary, and a free-carrier mobility of 0.1 cm<sup>2</sup>V<sup>-1</sup>s<sup>-1</sup> would imply a mean free  
23 electron path smaller than the interatomic distance. Therefore, the observed low electron mobility  
24 must be caused by trapping associated with the disk-like layers of the Cu-poor interfacial phase.  
25  
26 An alternative interpretation, arising from the performance of lamellar CuInS<sub>2</sub> photochemical  
27 electrodes by Cattarin et al.,<sup>25</sup> invokes barriers to charge transport. These authors find that the  
28 CuInS<sub>2</sub> bulk is *n*-type while the interphase lamellae are either insulating or *p*-type, such that they  
29 may form *n/i/n* or *n/p/n* barriers in the conduction band. Because the interphase layers in our crystal  
30 are so thin, any barrier to electron transport may not be built up by a space charge, but instead may  
31 be caused by an offset in the CB edges and/or by interface dipoles. Unfortunately, around room  
32  
33  
34  
35  
36  
37  
38  
39  
40  
41  
42  
43  
44  
45  
46  
47  
48  
49  
50  
51  
52  
53  
54  
55  
56  
57  
58  
59  
60

1  
2  
3 temperature the experimentally determined T-dependence of the mobility,  $\delta\mu_n/\delta T$ , is an unreliable  
4  
5 guide to a physical mechanism, as the transition from impurity scattering to lattice scattering can  
6  
7  
8 change the value and even the sign of  $\delta\mu_n/\delta T$ .<sup>27,49,55</sup>  
9

10 The electrical resistivity at room temperature (RT) of  $2.7 \times 10^6 \Omega\text{-cm}$  is high because of the  
11  
12 low electron mobility and the low electron concentration of  $2.3 \times 10^{13} \text{ cm}^{-3}$ . High resistivities have  
13  
14 been observed in as-grown crystals,<sup>22,55,70</sup> in crystals equilibrated with Zn (hence Cu-poor),<sup>27</sup> and  
15  
16 in thin films prepared without excess Cu.<sup>10,71</sup> As nanometer-thick Cu-poor interphases cannot be  
17  
18 detected by the routine X-ray diffraction analysis typically employed in thin-film solar cell work,  
19  
20 some of the highly resistive material of earlier studies also may have been stoichiometric  $\text{CuInS}_2$   
21  
22 with interphase inclusions. With the reservation that the thermal activation energy of the electrical  
23  
24 resistivity includes both electron density and mobility, the value measured here of 87 meV is  
25  
26 compatible with the donor ionization energies identified in  $\text{CuInS}_2$ , which range from 5 meV to  
27  
28  
29  
30  
31 570 meV.<sup>45,56-61</sup>  
32

33 The observations made on the present crystal agree with earlier work that invoked self-  
34  
35 compensation due to the additional degree of freedom inherent in a two-cation structure of  
36  
37 differing valency.<sup>51,58,72-74</sup> The widely accepted mechanism postulated by Zhang and Zunger<sup>45</sup> is  
38  
39 the formation of electrically neutral  $[\text{V}_{\text{Cu}}^{1-} \text{In}_{\text{Cu}}^{2+} \text{V}_{\text{Cu}}^{1-}]$  defect triplets, which the present study  
40  
41 confirms. Such self-compensation will raise the electrical resistivity. The sample's high resistivity  
42  
43 also suggests that the atomic ratio of  $\text{V}_{\text{Cu}}$  to  $\text{In}_i$ , estimated from EDS data to be 1.34, likely lies  
44  
45 very close to 2, as a large excess of relatively shallow  $\text{In}_i$  donors would greatly increase the  
46  
47 concentration of free electrons.<sup>56</sup>  
48  
49  
50

51 The spectral photoresponse, shown in SI Fig. S5, extends out to 1050 nm (1.18 eV)  
52  
53 illumination, and agrees with the photoconductivity spectrum reported by Cybulski et al.<sup>27</sup> for *n*-  
54  
55  
56  
57  
58  
59  
60

1  
2  
3 CuInS<sub>2</sub>. The corresponding deep levels most likely lie in the interphases and the partial dislocations  
4  
5 at their perimeters.  
6

7  
8 **4.5 Implications for CuInS<sub>2</sub> thin films.** The interphase layers segregate out on (112)  
9  
10 pseudo-twin boundaries, which are planar defects with very small interfacial energies.  
11  
12 Polycrystalline thin-film solar cells contain planar defects with substantially larger interfacial  
13  
14 energies, which are more conducive to the segregation of planar second phases: free surfaces  
15  
16 during film growth, grain boundaries, and device interfaces including heterojunctions and  
17  
18 electrical contacts. While such planar defects will be stable locations for Cu-poor interphases, these  
19  
20 can be detected only by high-resolution electron microscopy.<sup>33</sup> In the few-micrometer thick films  
21  
22 employed for solar cells, the Cu deficient material will not be sufficiently thick to reduce the  
23  
24 optical gap, and therefore won't be visible in optical absorption. However, in solar cell work to  
25  
26 date, many electrical effects have been imputed to native compositional inhomogeneities. To  
27  
28 establish reference samples, these electrical effects must be correlated once with structural and  
29  
30 compositional analysis on the nanometer scale. After that, electrical techniques will remain the  
31  
32 methods of choice for routine evaluation of device films. Electric fields associated with grain  
33  
34 boundaries including polarity-induced band bending may confine photogenerated minority  
35  
36 carriers, so that columnar grains will function as minority carrier conduits.<sup>51</sup> Using this argument,  
37  
38 Cu-depleted grain boundaries have been inferred from high minority carrier lifetime. On the other  
39  
40 hand, interphases at intra-grain boundaries may reduce the electron mobility as they do in the  
41  
42 single crystal. Copper-depleted layers are likely to form at solar cell heterojunctions. These may  
43  
44 favor or oppose the collection of photogenerated carriers. Indeed, CuInS<sub>2</sub> heterojunction solar cells  
45  
46 have been made more efficient by using buffer layers that are impervious to Cu-in-diffusion.  
47  
48 Pursuing a comparable goal on the Cu-rich side, CuInS<sub>2</sub> films have been deposited with excess Cu  
49  
50  
51  
52  
53  
54  
55  
56  
57  
58  
59  
60

1  
2  
3 and S to raise their chemical potentials above those in  $\text{CuInS}_2$ ; the ensuing macroscopic cover of  
4  
5 excess  $\text{Cu}_2\text{S}$  must be etched away before the heterojunction is formed.<sup>13</sup> Such empirical  
6  
7 approaches have been central to the development of thin-film chalcopyrite heterojunction solar  
8  
9 cells. Quantitative device design and simulation will require further experimental data, acquired  
10  
11 on the nanometer scale, about the properties of  $\text{CuInS}_2$  and of its interfaces with buffer and contact  
12  
13 materials.  
14  
15

## 16 17 **5. CONCLUSIONS & OUTLOOK**

18  
19 While the electrical transport properties of chalcopyrite-type semiconductors are adjusted by  
20  
21 changing stoichiometry instead of substitutional doping setting the solar cell performance of  
22  
23  $\text{CuInS}_2$  thin films by changing their Cu content has produced contradictory results. The present  
24  
25 study of a single crystal shows that ‘Cu-poor’  $\text{CuInS}_2$  is bi-phasic on the nanometer scale. Cu  
26  
27 deficiency segregates out readily along (112) pseudo-twin boundaries, where the deficiency  
28  
29 organizes in the form of  $[\text{V}_{\text{Cu}}^{1-} \text{In}_i^{2+} \text{V}_{\text{Cu}}^{1-}]$  defect triplets. These are electrically self-compensating  
30  
31 and neutral. In polycrystalline thin-film solar cells Cu-deficiency will similarly segregate, because  
32  
33 both Cu and In are fast diffusers at the substrate temperatures employed for solar cell fabrication.  
34  
35 Therefore, designing  $\text{CuInS}_2$  material for solar cells will need structural and compositional  
36  
37 information at the nanometer scale, acquired after both film growth and cell fabrication, coupled  
38  
39 with information on optical gap, band edge offsets and electrical transport properties. The present  
40  
41 study suggests three directions toward obtaining the needed quantitative understanding of, hence  
42  
43 better control over, this solar cell material. One is an exploration of type and magnitude of  
44  
45 electrical conductivity achievable by varying the sulfur pressure along the Cu-poor phase boundary  
46  
47 of  $\text{CuInS}_2$ . A second study would trace out the Cu-rich phase boundary in the same way. The result  
48  
49 would enable the quantitative design of the  $\text{CuInS}_2$  solar cell absorber layer. Coupled with these  
50  
51  
52  
53  
54  
55  
56  
57  
58  
59  
60



1  
2  
3 material studies, values of the ionization energy and electron affinity of the interphases are needed  
4  
5 to understand how they affect carrier transport properties as well as the open-circuit voltage of  
6  
7 solar cells made with bi-phasic material. The electron states of the interphase of the present study  
8  
9 may be quantum confined in the  $\langle 112 \rangle$  direction. Current research on  $\text{CuInS}_2$  (hence, non-toxic)  
10  
11 nanocrystals<sup>54</sup> and quantum dots<sup>75</sup> may extend to exploring their ordered-defect, Cu-deficient,  
12  
13 homologs, thereby helping to clarify band edge positions, quantized levels, and optical gaps.  
14  
15

## 16 ASSOCIATED CONTENT

17  
18  
19 **Supporting Information.** The supporting information is available free of charge at ###.

20  
21 Additional analysis and characterization of  $\text{CuInS}_2$  single crystal including: XPS analysis  
22  
23 of Cu 2p, In 3d, and S 2p (SI, Fig. S1); STEM-EDS mapping of Cu, In, and S (SI, Fig. S2);  
24  
25 EDS-measured atomic percent composition of Cu, In, and S (SI, Table S1); STEM-EDS  
26  
27 mapping of the single and double interphase layers in the  $\langle \bar{1}\bar{1}1 \rangle$  direction (SI, Fig. S3);  
28  
29 STEM-HAADF image showing two interfacial phases (SI, Fig. S4); and, additional  
30  
31 photoresponse data under 780 nm and 1050 nm illumination (SI, Fig. S5).  
32  
33  
34  
35

## 36 AUTHOR INFORMATION

### 37 38 39 **Corresponding Author**

40  
41  
42 \*E-mail: [jjfrick@stanford.edu](mailto:jjfrick@stanford.edu) (JJF); [wagner@princeton.edu](mailto:wagner@princeton.edu) (SW).  
43  
44

### 45 **Present Addresses**

46  
47 † Department of Aeronautics and Astronautics, Stanford University, Stanford CA 94305 (JJF);  
48  
49 MPA-MAG, Los Alamos National Laboratory, Los Alamos NM 87545 (SK).  
50  
51

### 52 53 **Author Contributions**

JJF and GC designed the experiments. JJF collected and analyzed electronic transport data with analysis assistance from RJC. JJF collected and analyzed photoconductivity data with analysis assistance from SW. GC collected and analyzed TEM data with analysis assistance from JJF and NY. JJF wrote the manuscript with assistance from GC, SW, and RJC. All authors have given approval to the final version of the manuscript.

## Notes

The authors declare no competing financial interest or other conflicts.

## ACKNOWLEDGMENT

This manuscript is based upon work supported by the National Science Foundation Graduate Research Fellowship via Grant 1656466 awarded to JJF. The crystal growth was supported by the ARO MURI on topological insulators, grant W911NF-1210461. The authors acknowledge the use of Princeton's Imaging and Analysis Center, which is partially supported by the Princeton Center for Complex Materials, a National Science Foundation (NSF)-MRSEC program (DMR-1420541). RJC acknowledges Grant DE-F602-98ER45706 and ABB acknowledges Grant DE-SC0002133 from the U.S. Department of Energy for financial support.

## REFERENCES

- (1) N.A. Goryunova. The Chemistry of Diamond-like Semiconductors; J.C. Anderson ed., Cambridge, Mass.: M.I.T. Press 1965.
- (2) Linus Pauling. Structure of Crystals. *Ind. Eng. Chem.* **1932**, *24*, 117.
- (3) Hahn, H.; Frank, G.; Klingler, W.; Meyer, A.-D.; Störger, G. Untersuchungen über ternäre Chalkogenide. V. Über einige ternäre Chalkogenide mit Chalkopyritstruktur. *Z. Anorg. Allg. Chem.* **1953**, *271* (3–4), 153–170.
- (4) Grimm, H. G.; Sommerfeld, A. Über den Zusammenhang des Abschlusses der Elektronengruppen im Atom mit den chemischen Valenzzahlen. *Z. Phys.* **1926**, *36* (1), 36–59.
- (5) H. M. Kasper. Crystal Growth and Properties of Some I-III-VI<sub>2</sub> Compounds. In *NBS Special Publication 364*; Washington DC, 1972; pp 671–679.

- 1
- 2
- 3
- 4 (6) Tell, B.; Shay, J. L.; Kasper, H. M. Room-Temperature Electrical Properties of Ten I-III-VI<sub>2</sub>
- 5 Semiconductors. *J. Appl. Phys.* **1972**, *43* (5), 2469–2470.
- 6
- 7 (7) Abrahams, S. C.; Bernstein, J. L. Piezoelectric Nonlinear Optic CuGaS<sub>2</sub> and CuInS<sub>2</sub> Crystal
- 8 Structure: Sublattice Distortion in A<sup>I</sup>B<sup>III</sup>C<sub>2</sub><sup>VI</sup> and A<sup>II</sup>B<sup>IV</sup>C<sub>2</sub><sup>V</sup> Type Chalcopyrites. *J. Chem.*
- 9 *Phys.* **1973**, *59* (10), 5415–5422.
- 10
- 11 (8) Shay, J. L.; Tell, B. Energy Band Structure of I–III–VI<sub>2</sub> Semiconductors. *Surf. Sci.* **1973**, *37*,
- 12 748–762.
- 13
- 14 (9) Hsu, T. M.; Lee, J. S.; Hwang, H. L. Photorefectance of Sulfur-annealed Copper Indium
- 15 Disulfide. *J. Appl. Phys.* **1990**, *68* (1), 283–287.
- 16
- 17 (10) Klenk, R.; Klaer, J.; Scheer, R.; Lux-Steiner, M. Ch.; Luck, I.; Meyer, N.; Rühle, U. Solar
- 18 Cells Based on CuInS<sub>2</sub>—an Overview. *Thin Solid Films* **2005**, *480–481*, 509–514.
- 19
- 20 (11) Kazmerski, L. L.; Sanborn, G. A. CuInS<sub>2</sub> Thin-film Homojunction Solar Cells. *J. Appl. Phys.*
- 21 **1977**, *48* (7), 3178–3180.
- 22
- 23 (12) Mitchell, K. W.; Eberspacher, C.; Cohen, F.; Avery, J.; Duran, G.; Bottenberg, W. Progress
- 24 towards High Efficiency Thin Film CdTe Solar Cells. *Solar Cells* **1988**, *23* (1), 49–57.
- 25
- 26 (13) Braunger, D.; Hariskos, D.; Walter, T.; Schock, H. W. An 11.4% Efficient Polycrystalline
- 27 Thin Film Solar Cell Based on CuInS<sub>2</sub> with a Cd-Free Buffer Layer. *Sol. Energ. Mat. Sol. C.*
- 28 **1996**, *40* (2), 97–102.
- 29
- 30 (14) AbuShama, J.; Noufi, R.; Johnston, S.; Ward, J.; Wu, X. Improved Performance in CuInSe<sub>2</sub>
- 31 and Surface-Modified CuGaSe<sub>2</sub> Solar Cells; Conf. Rec. 31<sup>st</sup> IEEE Photovoltaic Specialists
- 32 Conf. New York, 2005.
- 33
- 34 (15) Hiroi, H.; Iwata, Y.; Adachi, S.; Sugimoto, H.; Yamada, A. New World-Record Efficiency
- 35 for Pure-Sulfide Cu(In,Ga)S<sub>2</sub> Thin-Film Solar Cell with Cd-Free Buffer Layer via KCN-Free
- 36 Process. *IEEE J. Photovolt.* **2016**, *6* (3), 760–763.
- 37
- 38 (16) Nakamura, M.; Yamaguchi, K.; Kimoto, Y.; Yasaki, Y.; Kato, T.; Sugimoto, H. Cd-Free
- 39 Cu(In,Ga)(Se,S)<sub>2</sub> Thin-Film Solar Cell with Record Efficiency of 23.35%. *IEEE J. Photovolt.*
- 40 **2019**, *9* (6), 1863–1867.
- 41
- 42 (17) Seto, J. Y. W. The Electrical Properties of Polycrystalline Silicon Films. *J. Appl. Phys.* **1975**,
- 43 *46* (12), 5247–5254.
- 44
- 45 (18) Kamins, T. *Polycrystalline Silicon for Integrated Circuits and Displays*; Springer Science &
- 46 Business Media, 1998.
- 47
- 48 (19) Hwang, H. L.; Sun, C. Y.; Leu, C. Y.; Cheng, C. L.; Tu, C. C. Growth of CuInS<sub>2</sub> and its
- 49 Characterization. *Rev. Phys. Appl. (Paris)* **1978**, *13* (12), 745–751.
- 50
- 51 (20) Sun, C.; Hwang, H.; Leu, C.; Liu, L.; Tseng, B. Vapor Growth of CuInS<sub>2</sub> Single Crystals and
- 52 its Thermodynamic Considerations. *Jpn. J. Appl. Phys.* **1980**, *19* (S3), 81.
- 53
- 54 (21) Hsu, H. J.; Yang, M. H.; Tang, R. S.; Hsu, T. M.; Hwang, H. L. A Novel Method to Grow
- 55 Large CuInS<sub>2</sub> Single Crystals. *J. Cryst. Growth* **1984**, *70* (1), 427–432.
- 56
- 57 (22) Hsu, H. J.; Sun, C. Y.; Hwang, H. L. Growth of CuInS<sub>2</sub> Single Crystals by THM. *Electron.*
- 58 *Lett.* **1984**, *20* (9), 376.
- 59
- 60 (23) Fearheiley, M. L.; Dietz, N.; Lewerenz, H. J. Phase Relations in the Cu-In-S System and
- Growth of Large CuInS<sub>2</sub> Single Crystals. *J. Electrochem. Soc.* **1992**, *139* (2), 512–517.
- (24) Dietz, N.; Fearheiley, M. L.; Schroetter, S.; Lewerenz, H. J. Structural and Defect
- Characterization of CuInS<sub>2</sub> Single Crystals Grown under Elevated Pressures. *Mater. Sci. Eng.*
- B* **1992**, *14* (1), 101–109.

- 1  
2  
3  
4 (25) Cattarin, S.; Guerriero, P.; Razzini, G.; Lewerenz, H.-J. CuInS<sub>2</sub> with Lamellar Morphology:  
5 II . Photoelectrochemical Behavior of Heterogeneous Material. *J. Electrochem. Soc.* **1994**,  
6 *141* (5), 1100-1104.
- 7 (26) Cattarin, S.; Pagura, C.; Armelao, L.; Bertocello, R.; Dietz, N. Surface Characterization of  
8 CuInS<sub>2</sub> with Lamellar Morphology. *J. Electrochem. Soc.* **1995**, *142* (8), 2818-2023.
- 9 (27) Cybulski, D.; Opanowicz, A. Electrical and Photoelectrical Properties of *n*-CuInS<sub>2</sub> Single  
10 Crystals. *Cryst. Res. Tech.* **1997**, *32* (6), 813–820.
- 11 (28) Ivanov, V. A.; Viktorov, I. A.; Gremenok, V. F. Radiative and Photoelectric Properties of  
12 CuInS<sub>2</sub> Single Crystals. *Tech. Phys.* **2002**, *47* (9), 1197–1198.
- 13 (29) J. L. Shay; J. H. Wernick. *Ternary Chalcopyrite Semiconductors: Growth, Electronic*  
14 *Properties, and Applications*; Elsevier, 1975.
- 15 (30) Scheer, R.; Walter, T.; Schock, H. W.; Fearheiley, M. L.; Lewerenz, H. J. CuInS<sub>2</sub> Based Thin  
16 Film Solar Cell with 10.2% Efficiency. *Appl. Phys. Lett.* **1993**, *63* (24), 3294–3296.
- 17 (31) Mickelsen, R. A.; Chen, W. S. Development of a 9.4% Efficient Thin-Film CuInSe<sub>2</sub>/CdS  
18 Solar Cell; Conf. Rec. 15<sup>th</sup> IEEE Photovoltaic Specialists Conf. New York, 1981.
- 19 (32) Lomuscio, A.; Rödel, T.; Schwarz, T.; Gault, B.; Melchiorre, M.; Raabe, D.; Siebentritt, S.  
20 Quasi-Fermi-Level Splitting of Cu-Poor and Cu-Rich CuInS<sub>2</sub> Absorber Layers. *Phys. Rev.*  
21 *Applied* **2019**, *11* (5), 054052.
- 22 (33) Abou-Ras, D.; Kostorz, G.; Hariskos, D.; Menner, R.; Powalla, M.; Schorr, S.; Tiwari, A. N.  
23 Structural and Chemical Analyses of Sputtered In<sub>x</sub>S<sub>y</sub> Buffer Layers in Cu(In,Ga)Se<sub>2</sub> Thin-  
24 Film Solar Cells. *Thin Solid Films* **2009**, *517* (8), 2792–2798.
- 25 (34) Schmid, D.; Ruckh, M.; Grunwald, F.; Schock, H. W. Chalcopyrite/Defect Chalcopyrite  
26 Heterojunctions on the Basis of CuInSe<sub>2</sub>. *J. Appl. Phys.* **1993**, *73* (6), 2902–2909.
- 27 (35) Bär, M.; Klaer, J.; Weinhardt, L.; Wilks, R. G.; Krause, S.; Blum, M.; Yang, W.; Heske, C.;  
28 Schock, H.-W. Cu<sub>2-x</sub>S Surface Phases and Their Impact on the Electronic Structure of CuInS<sub>2</sub>  
29 Thin Films – A Hidden Parameter in Solar Cell Optimization. *Advan. Energ. Mater.* **2013**, *3*  
30 (6), 777–781.
- 31 (36) Bär, M.; Barreau, N.; Couzinié-Devy, F.; Weinhardt, L.; Wilks, R. G.; Kessler, J.; Heske, C.  
32 Impact of Annealing-Induced Intermixing on the Electronic Level Alignment at the  
33 In<sub>2</sub>S<sub>3</sub>/Cu(In,Ga)Se<sub>2</sub> Thin-Film Solar Cell Interface. *ACS Appl. Mater. Interfaces* **2016**, *8* (3),  
34 2120–2124.
- 35 (37) Ghorbani, E.; Erhart, P.; Albe, K. Energy Level Alignment of Cu(In, Ga) (S, Se)<sub>2</sub> Absorber  
36 Compounds with In<sub>2</sub>S<sub>3</sub>, NaIn<sub>5</sub>S<sub>8</sub>, and CuIn<sub>5</sub>S<sub>8</sub> Cd-Free Buffer Materials. *Phys. Rev. Materials*  
37 **2019**, *3* (7), 075401.
- 38 (38) Binsma, J. J. M.; Giling, L. J.; Bloem, J. Phase Relations in the System Cu<sub>2</sub>S-In<sub>2</sub>S<sub>3</sub>. *J. Cryst.*  
39 *Growth* **1980**, *50* (2), 429–436.
- 40 (39) Verheijen, A. W.; Giling, L. J.; Bloem, J. The Region of Existence of CuInS<sub>2</sub>. *Mater. Res.*  
41 *Bull.* **1979**, *14* (2), 237–240.
- 42 (40) Cattarin, S.; Dietz, N.; Lewerenz, H. J. CuInS<sub>2</sub> with Lamellar Morphology: I . Efficient  
43 Photoanodes in Acidic Polyiodide Medium. *J. Electrochem. Soc.* **1994**, *141* (5), 1095-1099.
- 44 (41) Thomere, A.; Guillot-Deudon, C.; Caldes, M. T.; Bodeux, R.; Barreau, N.; Jobic, S.; Lafond,  
45 A. Chemical Crystallographic Investigation on Cu<sub>2</sub>S-In<sub>2</sub>S<sub>3</sub>-Ga<sub>2</sub>S<sub>3</sub> Ternary System. *Thin Solid*  
46 *Films* **2018**, *665*, 46–50.
- 47 (42) Orlova, N. S.; Bodnar, I. V.; Kudritskaya, E. A. Crystal Growth and Properties of the CuIn<sub>5</sub>S<sub>8</sub>  
48 and AgIn<sub>5</sub>S<sub>8</sub> Compounds. *Cryst. Res. Tech.* **1998**, *33* (1), 37–42.
- 49  
50  
51  
52  
53  
54  
55  
56  
57  
58  
59  
60

- 1  
2  
3 (43) Qasrawi, A. F.; Gasanly, N. M. Photoelectronic and Electrical Properties of  $\text{CuIn}_5\text{S}_8$  Single  
4 Crystals. *Cryst. Res. Tech.* **2003**, *38* (12), 1063–1070.
- 5 (44) Ingo Österreicher. Oberflächenspektroskopische Charakterisierung von  $\text{CuInS}_2$ -  
6 Dünnschichten, PhD thesis, Justus-Liebig Universität, Giessen, Germany, 2003.
- 7 (45) Zhang, S. B.; Wei, S.-H.; Zunger, A.; Katayama-Yoshida, H. Defect Physics of the  $\text{CuInSe}_2$   
8 Chalcopyrite Semiconductor. *Phys. Rev. B* **1998**, *57* (16), 9642–9656.
- 9 (46) Wasim, S. M.; Rincón, C.; Marin, G.; Delgado, J. M. On the Band Gap Anomaly in I–III–  
10  $\text{VI}_2$ , I–III<sub>3</sub>– $\text{VI}_5$ , and I–III<sub>5</sub>– $\text{VI}_8$  Families of Cu Ternaries. *Appl. Phys. Lett.* **2000**, *77* (1), 94–  
11 96.
- 12 (47) Frick, J. J.; Kushwaha, S. K.; Cava, R. J.; Bocarsly, A. B. Characterization of Primary Carrier  
13 Transport Properties of the Light-Harvesting Chalcopyrite Semiconductors  $\text{CuIn}(\text{S}_{1-x}\text{Se}_x)_2$ . *J.*  
14 *Phys. Chem. C* **2017**, *121* (32), 17046–17052.
- 15 (48) Smyth, D. M. Thermodynamic Characterization of Ternary Compounds. I. The Case of  
16 Negligible Defect Association. *J. Solid State Chem.* **1976**, *16* (1), 73–81.
- 17 (49) Binsma, J. J. M.; Van Enkevort, W. J. P.; Staarink, G. W. M. CVT Growth of  $\text{CuInS}_2$  and  
18  $\text{CuGaS}_2$  Assisted by VLS Mechanisms. *J. Cryst. Growth* **1983**, *61* (1), 138–156.
- 19 (50) Wißmann, S.; Becker, K. D. Tracer Diffusion of Indium in  $\text{CuInS}_2$ . *Solid State Ionics* **1997**,  
20 *101–103*, 539–545.
- 21 (51) Persson, C.; Zunger, A. Compositionally Induced Valence-Band Offset at the Grain  
22 Boundary of Polycrystalline Chalcopyrites Creates a Hole Barrier. *Appl. Phys. Lett.* **2005**, *87*  
23 (21), 211904.
- 24 (52) Abou-Ras, D.; Schorr, S.; Schock, H. W. Grain-Size Distributions and Grain Boundaries of  
25 Chalcopyrite-Type Thin Films. *J. Appl. Crystallogr.* **2007**, *40* (5), 841–848.
- 26 (53) Rose, A. *Concepts in Photoconductivity and Allied Problems*; Interscience Publishers: New  
27 York, 1963.
- 28 (54) Houck, D. W.; Assaf, E. I.; Shin, H.; Greene, R. M.; Pernik, D. R.; Korgel, B. A. Pervasive  
29 Cation Vacancies and Antisite Defects in Copper Indium Diselenide ( $\text{CuInSe}_2$ ) Nanocrystals.  
30 *J. Phys. Chem. C* **2019**, *123* (14), 9544–9551.
- 31 (55) Look, D. C.; Manthuruthil, J. C. Electron and Hole Conductivity in  $\text{CuInS}_2$ . *J. Phys. Chem.*  
32 *Solids* **1976**, *37* (2), 173–180.
- 33 (56) Ueng, H. Y.; Hwang, H. L. The Defect Structure of  $\text{CuInS}_2$ . Part I: Intrinsic Defects. *J. Phys.*  
34 *Chem. Solids* **1989**, *50* (12), 1297–1305.
- 35 (57) Ueng, H. Y.; Hwang, H. L. The Defect Structure of  $\text{CuInS}_2$ . Part II: Thermal Annealing  
36 Defects. *J. Phys. Chem. Solids* **1990**, *51* (1), 1–10.
- 37 (58) Lany, S.; Zunger, A. Anion Vacancies as a Source of Persistent Photoconductivity in II–VI  
38 and Chalcopyrite Semiconductors. *Phys. Rev. B* **2005**, *72* (3).
- 39 (59) Rincón, C.; Márquez, R. Defect Physics of the  $\text{CuInSe}_2$  Chalcopyrite Semiconductor. *J. Phys.*  
40 *Chem. Solids* **1999**, *60* (11), 1865–1873.
- 41 (60) Chen, H.; Wang, C.-Y.; Wang, J.-T.; Hu, X.-P.; Zhou, S.-X. First-Principles Study of Point  
42 Defects in Solar Cell Semiconductor  $\text{CuInS}_2$ . *J. Appl. Phys.* **2012**, *112* (8), 084513.
- 43 (61) Cao, Q.; Gunawan, O.; Copel, M.; Reuter, K. B.; Chey, S. J.; Deline, V. R.; Mitzi, D. B.  
44 Defects in  $\text{Cu}(\text{In,Ga})\text{Se}_2$  Chalcopyrite Semiconductors: A Comparative Study of Material  
45 Properties, Defect States, and Photovoltaic Performance. *Advan. Energ. Mater.* **2011**, *1* (5),  
46 845–853.
- 47  
48  
49  
50  
51  
52  
53  
54  
55  
56  
57  
58  
59  
60

- 1  
2  
3 (62) Reynolds, S.; Brinza, M.; Benkhedir, M. L.; Adriaenssens, G. J. Photoconductivity in  
4 Materials Research. In *Springer Handbook of Electronic and Photonic Materials*; Kasap, S.,  
5 Capper, P., Eds.; Springer Handbooks; Springer International Publishing: Cham, 2017.
- 6 (63) Becker, K. D.; Wagner, S. Temperature-Dependent Nuclear Magnetic Resonance in  $\text{CuInX}_2$   
7 ( $X = \text{S, Se, Te}$ ) Chalcopyrite-Structure Compounds. *Phys. Rev. B* **1983**, *27* (9), 5240–5249.
- 8 (64) Scheer, R.; Lewerenz, H.-J. Formation of Secondary Phases in Evaporated  $\text{CuInS}_2$  Thin  
9 Films: A Surface Analytical Study. *J. Vac. Sci. Technol. A* **1995**, *13* (4), 1924–1929.
- 10 (65) Jaffe, J. E.; Zunger, A. Electronic Structure of the Ternary Chalcopyrite Semiconductors  
11  $\text{CuAlS}_2$ ,  $\text{CuGaS}_2$ ,  $\text{CuInS}_2$ ,  $\text{CuAlSe}_2$ ,  $\text{CuGaSe}_2$ , and  $\text{CuInSe}_2$ . *Phys. Rev. B* **1983**, *28* (10),  
12 5822–5847.
- 13 (66) Neumann, H.; Hörig, W.; Savelev, V.; Lagzdonis, J.; Schumann, B.; Kühn, G. The Optical  
14 Properties of  $\text{CuInS}_2$  Thin Films. *Thin Solid Films* **1981**, *79* (2), 167–171.
- 15 (67) Mobarak, M.; Shaban, H. T.; Elhady, A. F. Electrical and Thermoelectric Properties of  
16  $\text{CuInS}_2$  Single Crystals. *Mater. Chem. Phys.* **2008**, *109* (2), 287–290.
- 17 (68) Maeda, T.; Gong, W.; Wada, T. Crystallographic and Optical Properties and Band Structures  
18 of  $\text{CuInSe}_2$ ,  $\text{CuIn}_3\text{Se}_5$ , and  $\text{CuIn}_5\text{Se}_8$  Phases in Cu-Poor  $\text{Cu}_2\text{Se}$ – $\text{In}_2\text{Se}_3$  Pseudo-Binary System.  
19 *Jpn. J. Appl. Phys.* **2016**, *55* (4S), 04ES15, 1–10.
- 20 (69) Usujima, A.; Takeuchi, S.; Endo, S.; Irie, T. Optical and Electrical Properties of  $\text{CuIn}_5\text{S}_8$  and  
21  $\text{AgIn}_5\text{S}_8$  Single Crystals. *Jpn. J. Appl. Phys.* **1981**, *20* (7), L505.
- 22 (70) Bridenbaugh, P. M.; Migliorato, P. Junction Electroluminescence in  $\text{CuInS}_2$ . *Appl. Phys. Lett.*  
23 **1975**, *26* (8), 459–460.
- 24 (71) Herberholz, R.; Nadenau, V.; Rühle, U.; Köble, C.; Schock, H. W.; Dimmler, B. Prospects  
25 of Wide-Gap Chalcopyrites for Thin Film Photovoltaic Modules. *Sol. Energ. Mat. Sol. C.*  
26 **1997**, *49* (1), 227–237.
- 27 (72) Lany, S.; Zunger, A. Intrinsic D-X Centers in Ternary Chalcopyrite Semiconductors. *Phys.*  
28 *Rev. Lett.* **2008**, *100* (1) 016401.
- 29 (73) Zhao, Y.-J.; Persson, C.; Lany, S.; Zunger, A. Why Can  $\text{CuInSe}_2$  Be Readily Equilibrium-  
30 Doped  $n$ -Type but the Wider-Gap  $\text{CuGaSe}_2$  Cannot? *Appl. Phys. Lett.* **2004**, *85* (24), 5860–  
31 5862.
- 32 (74) Migliorato, P.; Shay, J. L.; Kasper, H. M.; Wagner, S. Analysis of the Electrical and  
33 Luminescent Properties of  $\text{CuInSe}_2$ . *J. Appl. Phys.* **1975**, *46* (4), 1777–1782.
- 34 (75) Fuhr, A.; Yun, H. J.; Crooker, S. A.; Klimov, V. I. Spectroscopic and Magneto-Optical  
35 Signatures of  $\text{Cu}^{1+}$  and  $\text{Cu}^{2+}$  Defects in Copper Indium Sulfide Quantum Dots. *ACS Nano*  
36 **2020**, *14* (2), 2212–2223.
- 37  
38  
39  
40  
41  
42  
43  
44  
45  
46  
47  
48  
49  
50  
51  
52  
53  
54  
55  
56  
57  
58  
59  
60

## TOC

